A Comparison of the Light Curves for NGC 4151

Melissa Hallum

A senior thesis submitted to the faculty of
Brigham Young University
in partial fulfillment of the requirements for the degree of

Bachelor of Science

Michael Joner, Advisor

Department of Physics and Astronomy

Brigham Young University

April 2017

ABSTRACT

A Comparison of the Light Curves for NGC 4151

Melissa Hallum
Department of Physics and Astronomy, BYU
Bachelor of Science

Reverberation mapping is a technique used to determine the mass of the supermassive black hole at the center of an active galaxy. The technique uses both photometry and spectroscopy. This project focuses on the photometry aspect of reverberation mapping and seeks to determine if the photometric method used will significantly affect the results. The light curves of NGC 4151 produced using AstroImageJ, IRAF, and ISIS are compared. IRAF and AstroImageJ use differential aperture photometry with comparison stars, while ISIS uses image subtraction photometry. ISIS yielded light curves different to those created from AstroImageJ and IRAF. Furthermore, due to errors from comparison stars, it is concluded that image subtraction photometry may be more accurate than differential aperture photometry for this galaxy.

Keywords: NGC 4151, reverberation mapping, super massive black holes, AGN, light curves, IRAF, AstroImageJ, ISIS

ACKNOWLEDGMENTS

Thank you to Dr. Joner, Dr. Jeffery, and Dr. Neilsen for their help and reviews.

Contents

List of Figures

Chapter 1

Introduction

The motivation for this paper is to refine the photometric part of reverberation mapping. Reverberation mapping is a tool used to determine the mass of the super massive black holes at the center of galaxies. This technique yields estimates of the mass of the central super massive black hole accurate to about a factor of three (Peterson 2003). However, accurate light curves are necessary for the results from reverberation mapping to be accurate. If different photometric techniques produce different light curves, the results from reverberation mapping would be different. Having an accurate mass of the central black hole is important because the mass must be accurate to about 10% in order to accurately study the energy of the active galactic nucleus (AGN) (Peterson 2003).

In this thesis, I sought to determine if image subtraction photometry is useful in creating a light curve of the active galaxy NGC 4151 (discussed in Section 1.1.3). Image subtraction photometry is often used for performing photometry of crowded fields (when there are many bright objects crowded together) in order to eliminate the excess light coming from the other objects. Because of the light from the surrounding galaxy, it can be difficult to measure the light flux from just the nucleus. I therefore chose to apply an image subtraction technique to a galaxy. To do this, I compared the light curves of NGC 4151 produced using three different programs: IRAF, AtroImageJ, and ISIS. AstroImageJ and IRAF both use comparison stars to produce light curves using differen-

tial aperture photometry. ISIS, on the other hand, uses an image subtraction technique to produce light curves. A comparison of the light curves is then used to determine the merit of using image subtraction photometry instead of differential aperture photometry.

This chapter is organized in the following manner: Section 1.1 includes a discussion on galaxies and NGC 4151. Section 1.2 explains the concepts behind reverberation mapping. Section 1.3 discusses differential aperture photometry and image subtraction photometry techniques. Finally, a complete overview of the remaining thesis is provided in Section 1.4.

1.1 Spectra and Galaxies

This section provides a detailed discussion on galaxies. To aid in the discussion on galactic spectra, Section 1.1.1 provides a brief explanation of spectral lines. Various types of galaxies are discussed in Section 1.1.2. Finally, NGC 4151, the subect of this thesis, is discussed in Section 1.1.3.

1.1.1 A Short Discussion on Spectra

A spectrometer analyzes the intensity of light from an object at a particular wavelength. A spectral line is formed when photons are absorbed or emitted by atoms. When atoms absorb photons, the intensity of light at the wavelength of the photons decreases, producing an absorption line. When atoms decay back to the ground sates, they emit photons, which increase the intensity of light at the wavelength of the photons, producing an emission line. Examples of spectral lines can be seen in Fig. 1.1. Furthermore, there are many factors that affect the width of an emission or absorption line. An example of a wider emission line, called a broad emission line, can also be seen in Fig. 1.1. Of particular interest for this discussion is Doppler broadening.

The motion of gas orbiting the center of a galaxy causes a Doppler shift in the light that we

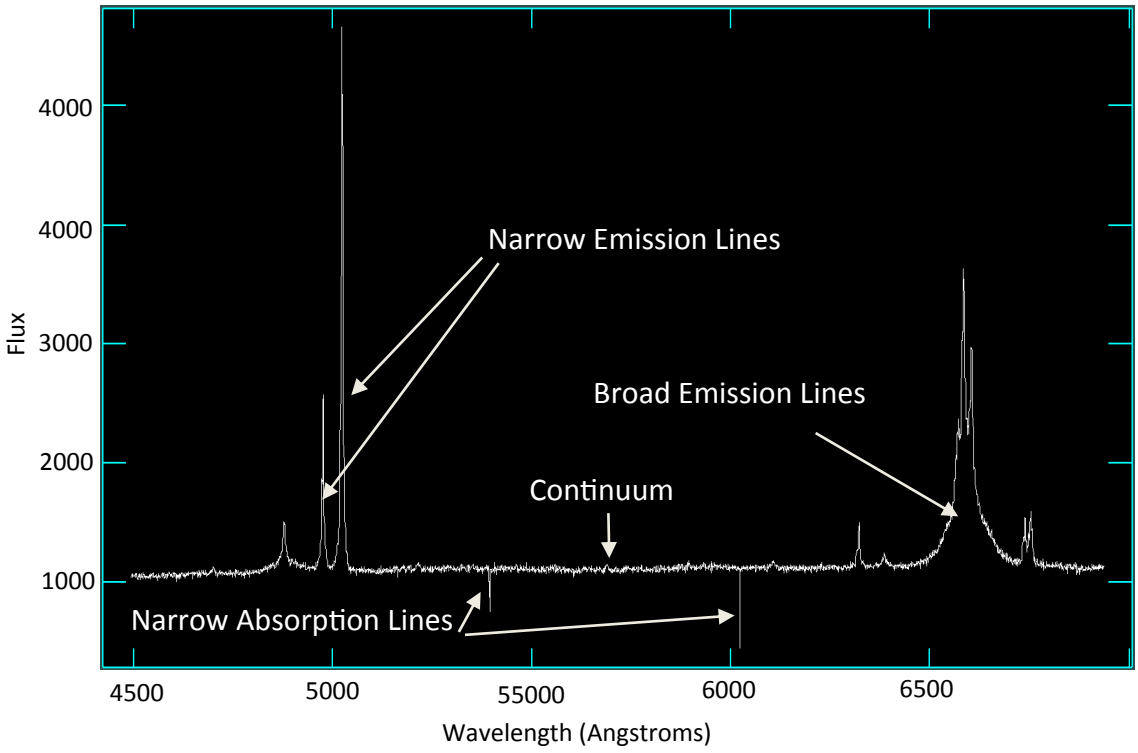

Figure 1.1 Spectrum of NGC 4151 that was given to me by Dr. Hintz (Hintz 2017). The data was taken from the Dominion Astrophysical Observatory. Examples of emission lines versus absorption lines, and narrow lines versus broad lines are indicated.

observe. This movement broadens spectral lines by the amount $\Delta\lambda$:

$$\Delta\lambda \approx \frac{2\lambda v}{c}, \tag{1.1}$$

where λ is the wavelength of the spectral line, v is the velocity of the orbiting gas, and c is the speed of light (Carroll & Ostlie 2007). In the case of an active galaxy, Doppler broadening of the spectral lines is caused rapidly orbiting gas clouds that are relatively close to the center of the AGN. For this reason, these clouds are called broad line region clouds. The area that they occupy is referred to as the broad line region (BLR). The importance of the BLR will be discussed in Section 1.2.

1.1.2 Galaxies and AGN

Galaxies exist in many different shapes and forms. There are three main classifications for galaxies: spiral, elliptical, and irregular. Because a spiral galaxy is the subject of this thesis, we will discuss spiral galaxies further. A spiral galaxy has spiral arms rotating around a central bulge. The intensity of the surface brightness, I, of a spiral galaxy usually follows the rule

$$\log I \propto -r, \tag{1.2}$$

where r is the distance from the center of the galaxy to the observer (Ryden & Peterson 2010a). For most spiral galaxies, this light comes primarily from the stars that make up the galaxy. Active galaxies, however, have another source of light.

An active galaxy is a galaxy whose luminosity output changes with time. Active galaxies make up only about 10% of all galaxies (W. M. Keck Observatory Accessed January 24, 2017). They can be recognized by their strong emission lines due to a large amount of hot gas, which indicates a significant amount of non-stellar light (Ryden & Peterson 2010a). This non-stellar light comes from its central nucleus, which is called an active galactic nucleus (AGN) (Ryden & Peterson

2010a). The source of this light is the accretion disk surrounding a supermassive black hole and is discussed in Section 1.2. Like normal galaxies, active galaxies are categorized.

There are three major classes of active galaxies: blazars, Seyferts, and quasars. However, it is believed that the different classes of active galaxies are all the same object viewed from different angles. A model of a typical AGN can be seen in Fig. 1.2. A blazar is seen from a line of sight coming from the jets. A Seyfert galaxy is seen from the side without the jets in view. Additionally, there are two types of Seyfert galaxies, Seyfert I and Seyfert II. A Seyfert I galaxy includes a view containing both the broad and narrow line regions. (The narrow line region indicates the areas from which narrow spectral lines are produced.) The line of sight for a Seyfert II galaxy is such that the dusty torus obscures the BLR, thus, only the narrow line produced by the slower moving narrow line region clouds are visible. Quasars are active galaxies viewed from a variety of angles. Additionally, Seyfert galaxies are very similar to quasars, and are sometimes considered a type of quasar. It is therefore important to discuss the similarities and differences between these two types of AGN's.

Quasars are extremely bright, distant radio sources with broad emission lines. The light of most quasars varies by about 0.3-0.5 magnitudes over a time period of a few months, but some can vary on a time scale of just a few days (Peterson 1997). Quasars are one of the only objects that can be detected at a high z value ($z > 1$) (Peterson 1997). A high z value indicates a great distance. Quasars are therefore important for the study of distant objects, as are Seyfert galaxies.

The luminosity of Seyfert galaxies is lower than that of quasars, and they tend to be less distant (Ryden & Peterson 2010b). Their nuclei are similar, but the host galaxy is noticeably detectable for Seyfert galaxies, whereas a quasar is usually unresolved from ground based observations (Peterson 1997). Seyfert galaxies were discovered by Carl Seyfert in the 1940s (Ryden & Peterson 2010b). He studied the optical spectra of several AGN, including NGC 4151, and noticed the presence of broad emission lines (Peterson 1997). Seyfert galaxies are thus categorized by their strong, high-

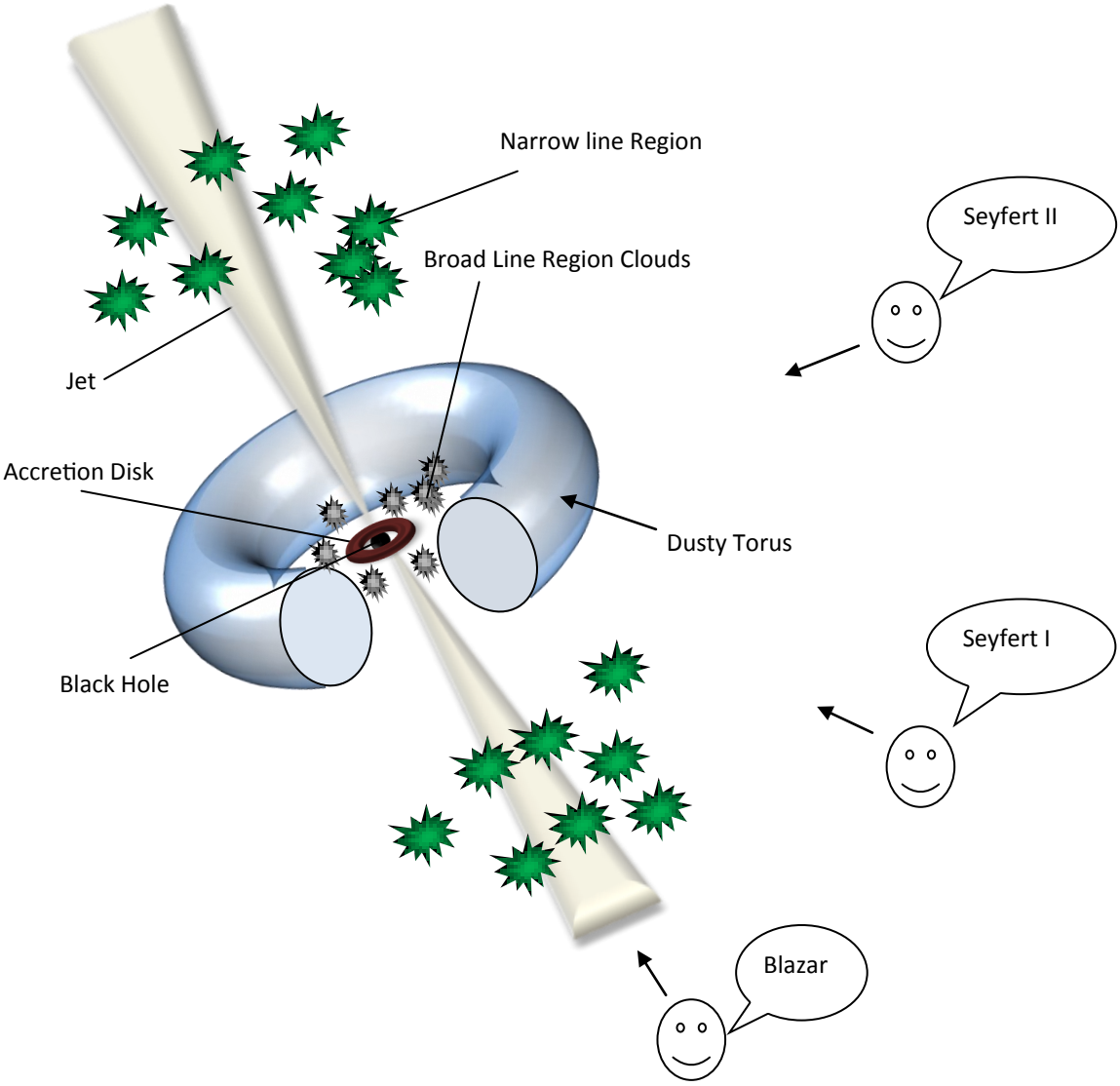

Figure 1.2 A model of an active galactic nucleus. The accretion disk is the material circling the black hole at the center. It is the source of the AGN luminosity. The broad line region clouds produce broad spectral lines. The narrow line region clouds produce narrow spectral lines. A blazar is seen from a line of sight coming from the jets. A Seyfert galaxy is seen from the side without the jets in view. Seyfert I galaxies include a view containing both the broad and narrow line regions, while Seyfert II galaxies include a view of only the narrow line region because the dusty torus blocks the view of the BLR. Based on image from NASA (Accessed February 6, 2107).

ionizing emission lines and weak absorption lines (Peterson 1997). Seyfert spectra are similar to quasar spectra. The difference is that for a quasar, the stellar absorption is typically weaker than for Seyfert galaxies, and the narrow emission lines are usually weaker than the broad lines (Peterson 1997). In summary, the main differences between quasars and Seyfert galaxies are that the Seyfert galaxies are less active, less luminous, and have smaller super massive black holes at their cores.

1.1.3 NGC 4151

NGC 4151, also known as "The Eye of Sauron" (Chandra X-Ray Observatory Accessed February 6, 2017), is the subject of this thesis. It is a classical Seyfert 1 galaxy (Holt et al. 1980), and is often referred to as an "archetypical Seyfert 1 galaxy" (Keck et al. 2015). It is located in the Canes Venatici constellation, about 43 million light years away from the Earth (Chandra X-Ray Observatory Accessed February 6, 2017). Despite this distance, it is one of the closest active galaxies, with $z = 0.0033$ (Couto et al. 2016). It is also one of the brightest AGN in the sky (Wildy et al. 2016), with a bolometric luminosity of about 5×10^{43} erg s^{-1} (Keck et al. 2015). This closeness and brightness makes it an ideal object to study. Past studies have determined a mass of 4.57×10^7 solar masses for the black hole at the center of the galaxy (Bentz et al. 2006). Despite the extensive studies on NGC 4151, there remains some unknowns. For example, there are still many unknowns regarding the spin of the the black hole at the center of the galaxy (Keck et al. 2015). More studies regarding NGC 4151 are therefore needed.

1.2 Black Holes Masses and Reverberation Mapping

A black hole is an object so massive that not even light can escape its gravitational pull. Because light cannot escape a black hole, it cannot be seen. Therefore, the gravitational effects of the black hole on surrounding material are used to study black holes. Because black holes play a role in

galaxy evolution, determining the mass of the black hole is of utmost importance. This section discusses some methods used to determine the mass of black holes at the center of active galaxies.

Super-massive black holes have been found in the center of almost every galaxy, active or normal (Slater & Freedman 2012). In 1968, Donald Lynden Bell theorized that a super-massive black hole at the center of an AGN is the source of the variability in the AGN (Slater & Freedman 2012). As material falls into a black hole, it forms an accretion disk, much like water circling a drain. The falling gas from the accretion disk produces the varying radiation. The properties of the accretion disk and the produced radiation are highly dependent on the mass of the black hole.

The black hole at the center of an active galaxy must be extremely large, on the order of more than a million times the mass of the Sun (Schödel et al. 2002). This is known from the Eddington limit, the limit of how fast a compact object can accumulate mass. It is a basic way of getting an idea of the mass of the central black hole and is defined as,

$$L_{\rm Edd} = 30,000(M/M_{\odot})L_{\odot}, \tag{1.3}$$

where $L_{\rm Edd}$ is the maximum luminosity produced by the object, M is the mass of the object (the black hole), $M_{\odot}$ is the mass of the Sun, and $L_{\odot}$ is the luminosity of the sun (Slater & Freedman 2012). In the case of black holes, $L_{\rm Edd}$ comes from the accretion disk surrounding the black hole. If we measure the luminosity coming from an AGN, we can then use Eq. 1.3 to estimate the mass of the central black hole. Because galaxies are quite luminous, from the Eddington limit, we know that the super-massive black holes powering AGN's must be extremely massive. However, it is difficult to determine the exact mass of these black holes.

One limitation to determining the exact mass of a black hole is that the gravitational effects on the gas and dust dynamics are seen only on a fairly small scale (Ryden & Peterson 2010a). These effects extend only to the radius of influence, $r_{\rm bh}$, which is defined as

$$r_{\rm bh} = GM_{bh}/\sigma_*^2, \tag{1.4}$$

where $M_{\rm bh}$ is the mass of the black hole and σ_* is the velocity dispersion of the stars in the central bulge, and G is the gravitational constant (Ryden & Peterson 2010a). This limitation makes finding the mass of the central black hole from the orbit of stars around the center of a galaxy difficult because one would need a telescope with very high resolution to resolve the individual stars close to the center of the galaxy.

The orbits of stars close to the center of our Galaxy have been used to find the mass of the central black hole. Ghez et al. (2002) used the orbit of S2, the star closest to Sagittarius A* (the supermassive black hole at the center of the Milky Way) to determine properties of the central black hole. The orbital parameters of an orbiting star tell us about the gravitational well produced by the unseen compact object, and thus its mass. Using this method, Ghez et al. determined that S2 orbited an enclosed mass of $4.1 \pm 0.6 \times 10^6 M_\odot$ (Ghez et al. 2002). A drawback to this method is that the orbit of stars around the center of the galaxy can be extremely long. For example, S2 has an orbital period of 15.2 years (Schödel et al. 2002). Observing a star over this length of time, or longer, is impractical.

A faster similar way to determine the mass of a central black hole is through the Doppler shift from groups of stars. For example, the mass of the black hole in the Andromeda Galaxy, the galaxy closest to our Galaxy, was measured in the 1930s through the spectroscopic Doppler shifts of the stars near the center of the galaxy (Slater & Freedman 2012). From these spectroscopic Doppler shifts, the orbital speeds of the stars can be computed. The mass of the black hole orbited by these stars can then be determined from these orbital speeds. This method indicates that the black hole at the center of the Andromeda has a mass of about $3 \times 10^7 M_\odot$ (Slater & Freedman 2012). The drawback to this method, however, is that, unlike the previous method, it requires the study of several stars (Slater & Freedman 2012). Either using direct observations of the orbits of resolved central stars or using their Doppler shifts to find the velocity dispersions are difficult methods to use on distant galaxies due to the difficulty in resolving individual stars. Reverberation mapping is

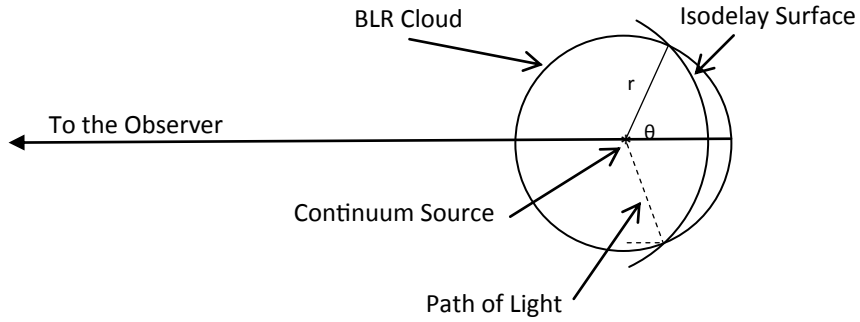

Figure 1.3 A model of the BLR, where r indicates the radius of the BLR clouds and the dotted lines represent the path of a photon. Light takes time to travel from the continuum in the center to the BLR clouds This time lag is used in reverberation mapping to find the mass of the central black hole. The continuum source is assumed to be very small compared to the BLR clouds. It is also assumed that photons travel unhindered at the speed of light until they are absorbed by particles in the BLR cloud (Peterson 1997). Adapted from (Peterson 1997)

a more accessible way of determining the mass of the supermassive black hole at the center of an active galaxy.

Reverberation mapping is a technique used to study the BLR of an AGN to gain information about the central black hole. This method is possible because the kinematics of the BLR are largely determined by the gravity and radiation pressure produced by the central source (the black hole). The broad emission lines are produced from photoionization of the BLR clouds by the radiation from the accretion disk of the black hole. The BLR cloud velocities causing the Doppler broadening of the emission lines (see Section 1.1.1) vary from $\Delta v_{fwhm} \approx 500$ km/s to more than 10^4 km/s (Peterson 1997). The key to reverberation mapping is that the emission lines from the BLR respond to a change in the continuum, but this response is delayed due to the time it takes the light to travel.

Light takes time to travel from the continuum in the center to the BLR clouds. The continuum is assumed to be one central source that is small in size compared to the distance to BLR, as indicated in Fig. 1.3. As a change occurs in the continuum, the resulting change in light must travel to the

BLR clouds. It is further assumed that the light from the continuum reaches the BLR cloud on a time scale shorter than the time scale of other geometric changes in the broad line region (Peterson 1997). Therefore, the time delay used in reverberation mapping is due to a change only in the continuum and not due to other factors. When the photons reach the BLR, the BLR clouds absorb the photons and then re-emit the radiation on an almost instantaneous time scale (Peterson 1997). The time delay, τ, between the emission of light from the continuum source (the accretion disk) and when that light reaches the BLR, is related to the distance from the black hole to the BLR, r, by

$$\tau = (1+\cos(\theta))r/c, \tag{1.5}$$

where θ is indicated in Fig. 1.3, and c is the speed of light (Peterson 1997). This time delay is backbone of the mathematics of reverberation mapping.

The time delay, τ, can be found using the continuum light curve, $C(\tau)$, and the emission-line light curve, $L(\tau)$, to find the transfer function, $\Psi(\tau)$. The continuum light curve (from near the black hole), the emission-line light curve (from the BLR clouds), and the transfer function are related through the transfer equation,

$$L(t) = \int_{-\infty}^{\infty} \Psi(\tau)C(t-\tau)d\tau \tag{1.6}$$

(Peterson 1997). After solving for $\Psi(\tau)$, the equation,

$$\Psi(\tau)d\tau = 2\pi\zeta rcd\tau, \tag{1.7}$$

where ζ is a constant, is used to find τ (Peterson 1997). Once τ is found, the mass of the black hole can be found using a simple energy relation.

We begin with the viral theorem

$$K = -\frac{U}{2}, \tag{1.8}$$

where K is the average kinetic energy of the BLR clouds, and U is the average gravitational potential energy. Note that

$$K = \frac{1}{2}mv^2, \tag{1.9}$$

where m is the average mass of the BLR clouds and v is the average velocity of the BLR clouds, which is found from the width of the Doppler broadened spectral lines. Also note that

$$U = -\frac{GMm}{r^2}, \tag{1.10}$$

where M is the mass of the black hole, m is the average mass of the BLR clouds, G is the gravitational constant, and r is the distance from the black hole to the BLR. Substituting Eq. 1.9 and Eq. 1.10 into Eq. 1.8 yields

$$mv^2 = \frac{GMm}{r^2}, \tag{1.11}$$

so

$$M = \frac{v^2 r}{G}. \tag{1.12}$$

Since r is the distance that the light travels between leaving the accretion disk and arriving at the BLR,

$$r = c\tau, \tag{1.13}$$

where c is the speed of light. Thus,

$$M = \frac{v^2 c\tau}{G}. \tag{1.14}$$

To account for the orientation of the galaxy a scaling factor, f, is used. Thus,

$$M_{BH} = f\frac{v^2 c\tau}{G}. \tag{1.15}$$

Therefore, reverberation mapping, in which τ and Δv are found, leads us to an estimate of the mass of the central black hole.

1.3 Photometric Techniques and Programs

IRAF, AstroImageJ, and ISIS are programs used to generate light curves. A light curve is a plot of light output verses time. IRAF, the Image Reduction and Analysis Facility, is a software distributed by the National Optical Astronomy Observatories (NOAO) (Tody 1993). It can be used to reduce raw images and perform photometry. ImageJ is an open source software created by Wayne Rasband (Scheider et al. 2012). AstoImageJ (AIJ) is a variation of ImageJ specific to astronomy created by Karen Collins and John Kielkopf (Collins et al. 2017). Like IRAF, it can be used to perform photometry. AstoImageJ and IRAF both produce light curves using differential aperture photometry. In aperture photometry, the change in the amount of light coming from a source is determined by comparing the number of photons coming from the source to that coming from the comparison stars. ISIS, Image Subtraction Image Subtraction, is a package created by Christofe Alard and C. Lupton used to perform image subtraction photometry (Alard & Lupton 1998). In image subtraction photometry, comparison stars are not used. Instead, a reference frame is created and is then subtracted from each image so that only the changing light remains. A comparison of the light curves produced by these different techniques, differential aperture and image subtraction photometry, is the focus of this thesis.

1.4 Thesis Overview

The remainder of this thesis discusses the carrying out of the project and the results. Chapter 2 recounts the observations, the processing of the images obtained, and the production of the light curves. The light curves in the V filter are presented in Chapter 3. The light curves in the B, I, R, and WA filters are included in Appendix A. The results and future work are also discussed in Chapter 3.

Chapter 2

Observations and Processing

This chapter explains how the images where obtained and processed. Section 2.1 goes over the observations made. Section 2.2 explains how the images were processed. Finally, Section 2.3 describes the process of creating the light curves.

2.1 Observations

All data was gathered from the West Mountain Observatory near Provo, Utah during the summer of 2016. The Observatory is owned by Brigham Young University and houses a 0.32-meter telescope and a 0.9-meter telescope. All observations were done using the 0.9-meter telescope and a charged coupling device (CCD). A CCD is a light detector. It counts the number of photons hitting each pixel over a period of time referred to as the exposure time. The exposure times ranged from 30 seconds to 120 seconds. A summary of the observations and exposure times can be found in Appendix B. The telescope has a focal ratio of f/5.5, with a focal length of 5029 mm. The CCD has a plate scale of 0.61 arcsec/pix and is 2048 x 2048 pixels in size. The images where trimmed during processing to 2000 x 2000 pixels. Using

$$\theta = s \times d, \tag{2.1}$$

where s is the plate scale and d is the length of the CCD, yields a field of view of 20.3 arcminutes per side for this configuration. This combination thus produces an image covering about 412 square arcmin of the sky. Bandpass filters were also used to analyse the flux of light within specific wavelength intervals.

The Cousins/Johnson B, V, R, and I filters and a Wide H-alpha (WA) filter were used for the individual observations. Filters are used to allow only light within a certain wavelength range to pass through. The B, V, R, and I filters correspond respectively to light with blue, green, red, and near infrared wavelengths. The WA filter is centered on the Balmer alpha line, 6563 Angstroms, and the pass band is 21 nm. As discussed in the previous chapter, the time lag between filters are key to reverberation mapping because the continuum produces light at a wavelength different from the wavelength of light produced by the BLR. However, due the length of this thesis, only the light curve in the V filter will be examined in detail. Light curves in the B, R, I, and WA filters are found in Appendix B. A summary of the dates, exposure times, and filters used for each image can be found in Appendix B.

2.2 Processing Raw Data

IRAF was used to remove instrumental noise from the raw images. When an image is taken with a CCD, there are three principal sources of noise that must be corrected using three types calibration images. The bias frame is an exposure taken for zero seconds. This frame accounts for the intrinsic noise stored in the CCD itself. The bias frame is used in calibration by subtracting it from each image. The dark frame is an exposure taken with the telescope closed for a duration comparable to the exposure times used for the each of the images. This frame accounts for the thermal noise produced by the CCD. The dark frame is used in calibration by subtracting it from each image. The flat frame is an exposure taken in each filter with the telescope pointed at a part of the sky

Figure 2.1 A raw image (left) and a reduced image (right). The reduced image is smoother than the raw image.

that is as smooth as possible, either at sunrise or at sunset. This frame accounts for the different reactions to light of the pixels in the CCD. The flat frame is applied in calibration by dividing each image by the normalized flat frame for the same filter. The application of these calibration frames creates a reduced image. A comparison of a raw image and a reduced image can be seen in Fig. 2.1. The reduced images have minimal instrumental noise and are one step closer to being ready for photometry.

2.3 Light Curve Creation

Several steps were necessary to make the reduced images ready for photometry. I first used a package created by Dr. Jeffery to shift the images so that they were aligned (Jeffery 2016). This code can be found in Appendix C. To account for exposure time variations, I used the imarith package in IRAF to divide each image by its exposure time. I then multiplied each image by the shortest exposure time used for images in the same filter. In order to find the average over a night

of observations, I used the imarith package again to add all images from the same day, and in the same filter, together and then divide by the number of images combined. These steps produced one image per night in each filter that is aligned and has exposure time consistent with the other images.

After preparing the images, my next step was to choose comparison stars and reference frames. As explained in section 1.3, IRAF and AIJ require comparison stars. I chose comparison stars whose light output remained constant and were of comparable brightness and color to the center of the galaxy. The chosen stars are indicated in Fig. 2.2. Instead of comparison stars, ISIS requires a list of reference frames. These reference frames are combined to create a master reference frame. I chose the reference frames based on which frames had the best seeing. Seeing refers to the full-width at half-max (FWHM) of the stars. For each frame, I measured the FWHM of several different stars to find an average for each frame. I then chose the frames with the smallest full-width-half-max as the reference frames. The chosen reference frames were 20160421_NGC4151-V.fits, 20160602_NGC4151-V.fits, 20160604_NGC4151-V.fits, 20160605_NGC4151-V.fits. Each image is then subtracted from the master reference frame to produce a subtracted image. These images are then added together to produce a combined subtracted image. The combined subtracted image in the V filter can be seen in Fig. 2.3. The combined subtracted images in the other filters can be found in Appendix A. The white spots in the subtracted image indicate fluctuations. There is a small, but distinct white spot at the center of the galaxy. This means that the light output is fluctuating. The other white spots are mostly due to either noise or saturated pixels in the vicinity of bright stars, and do not affect the results.

Each of the photometry methods used requires a choice of aperture size. For each method, 20 pixels for the inner radius and 25 pixels for the outer radius was used for the sky annulus. The object aperture radius was determined by experimentation. As the aperture size increases, more light from the object is included. At a certain point, there is only sky noise being added. Light curves

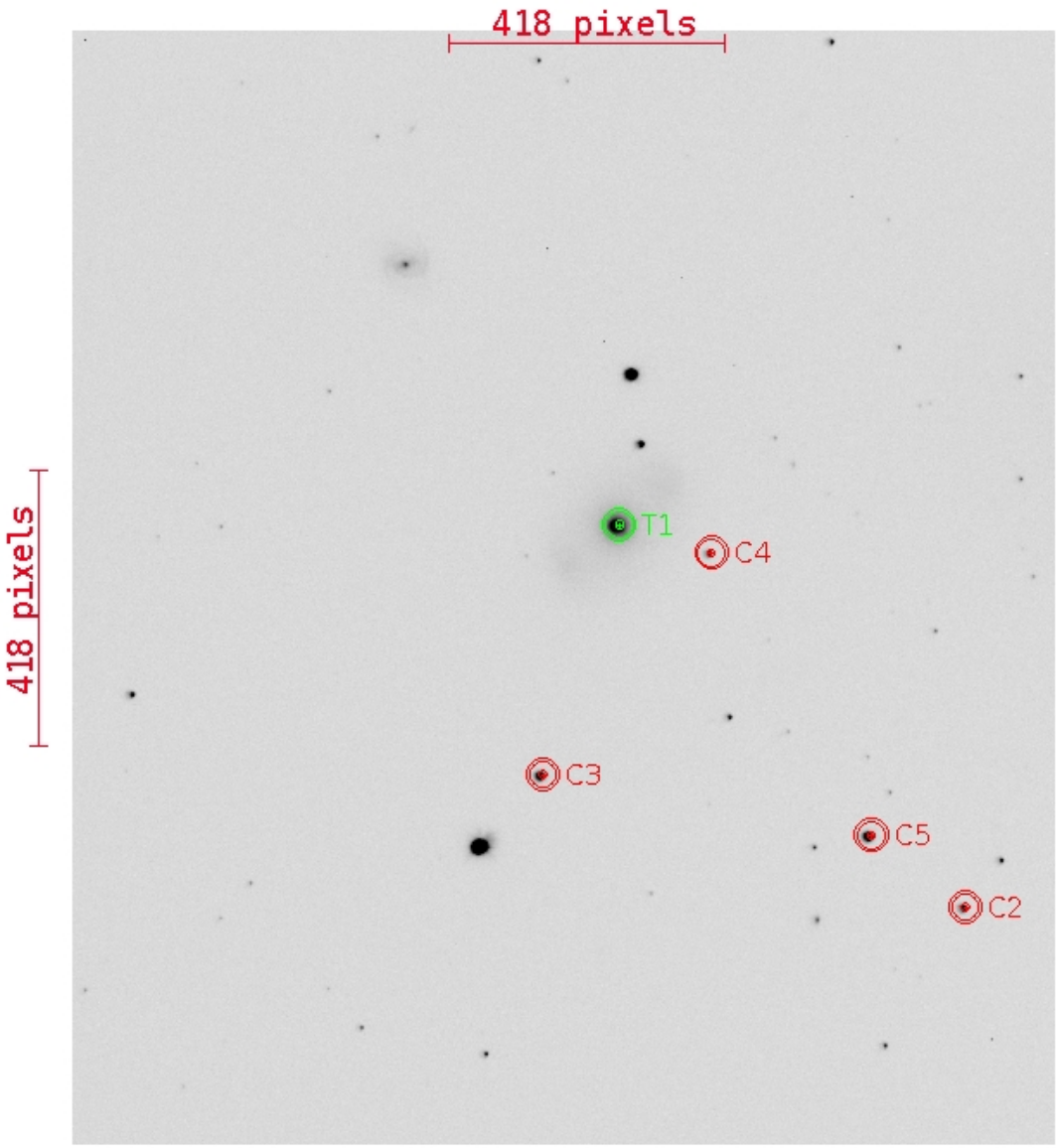

Figure 2.2 An image of the field in the V filter showing the apertures used for photometry. An inner radius of 20 pixels and an outer radius of 25 pixels were used for the sky annulus, and a radius of 6 pixels was used for the object aperture. The green aperture indicates NGC 4151. The red apertures indicate the comparison stars.

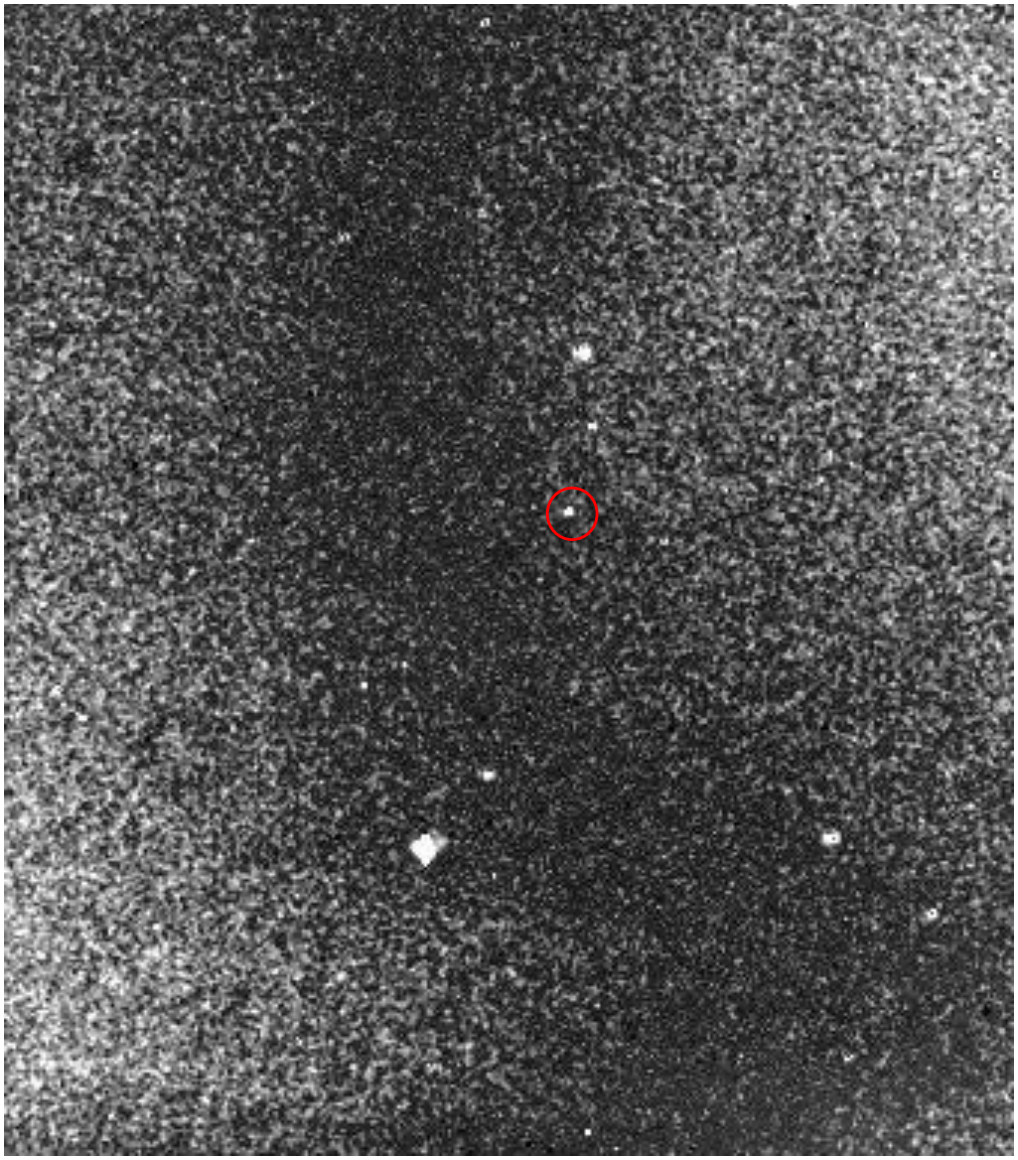

Figure 2.3 The combined subtracted image in the V filter produced by ISIS. The bright spots indicate the points of variation. As we can see, there is some noise in the frame. Additionally, there are a few bright spots produced by saturated star images. However, these do not affect our results for the galaxy. The location of the nucleus of the galaxy is indicated by the red circle. Notice the bright spot indicating a changing light flux.

using aperture radii sizes ranging from 2-10 pixels with the V filter using IRAF are presented in Figure 2.4. Notice that that as the aperture size increases, the light curve changes significantly due to the increase of light enclosed. At a certain point, however, the object is completely included in the aperture. An increase in aperture size thus only augments the noise, and the light curve only changes by a small amount each time the aperture is increased. Examination of these graphs show that the the light curve becomes steady around a radius of six or seven pixels. A table of the average magnitude and the standard deviation for each apertures size is presented in Table 2.1. These values are then graphed in Figure 2.5. Notice that after an aperture radius of about six or seven pixels, the change in magnitude begins to decrease. (Keep in mind that magnitude is a logarithmic scale.) Choosing an aperture size that includes minimal surrounding light is especially important for galaxies because the non-fluctuating, light from the surrounding galaxy can dominate the fluctuating light from the nucleus, smoothing the light curve. This process justifies the choice of an aperture radius of six pixels as the aperture radius that includes the entire object with minimal sky light. The apertures can be seen in respect to the objects in Fig. 2.2 for IRAF and AstroImageJ, and Fig. 2.6 for ISIS.

With these parameters, I used IRAF, AIJ, and ISIS to create the light curves. AIJ produces results already in units of apparent magnitude, but IRAF and ISIS do not. The light curves produced by IRAF are in differential magnitude. Dr. Joner provided standardized values for the comparison stars, which can be found in Table 2.2 (Joner 2017). I converted the differential magnitude produced by IRAF to apparent magnitude by adding the average of the standardized magnitudes for each comparison star. The light curves produced by ISIS are in units of flux. The process used to convert flux to magnitude is slightly more complicated and is therefore explained separately in Section 2.3.1. The apparent magnitude light curves in the V filter are presented in Chapter 3, and the light curves in the other filters can be found in Appendix A.

The average magnitudes and errors of NGC 4151 and the comparison stars in the V filter from

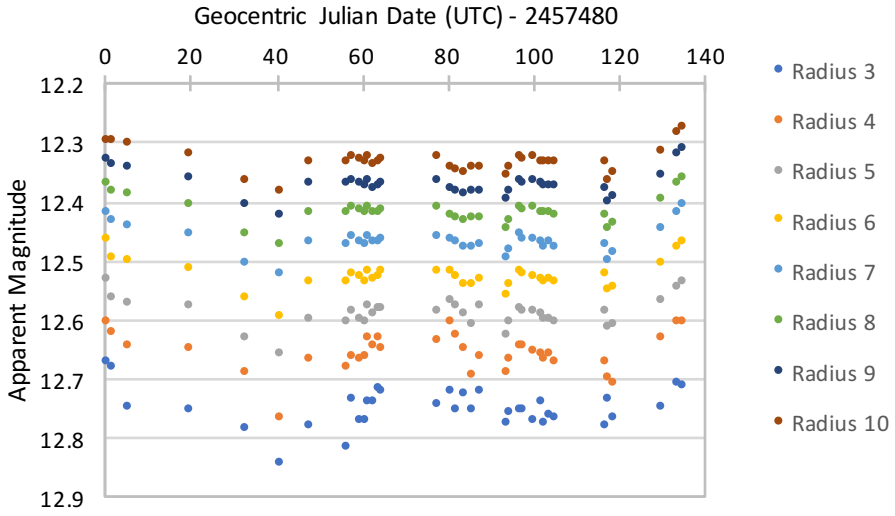

Figure 2.4 Light curves of NGC 4151 in the V filter using AstroImageJ with different aperture radii (in pixels). Notice that that as the aperture size increases, the light curve changes significantly due to the increase of light enclosed. At a certain point, however, the object is completely included in the aperture. An increase in the aperture radius thus only augments the noise, and the light curve only changes by a small amount each time the aperture is increased. Examination of these graphs show that the the light curve becomes steady around a radius of six pixels.

Table 2.1 Average magnitude and standard deviation for various aperture radii in the V filter using AIJ. (See Fig. 2.5 for plot

Aperture Radius (Pixels)	Average Magnitude	Average Error
3	12.752	0.0033
4	12.658	0.0029
5	12.590	0.0027
6	12.527	0.0026
7	12.467	0.0025
8	12.417	0.0025
9	12.371	0.0025
10	12.332	0.0025

.)

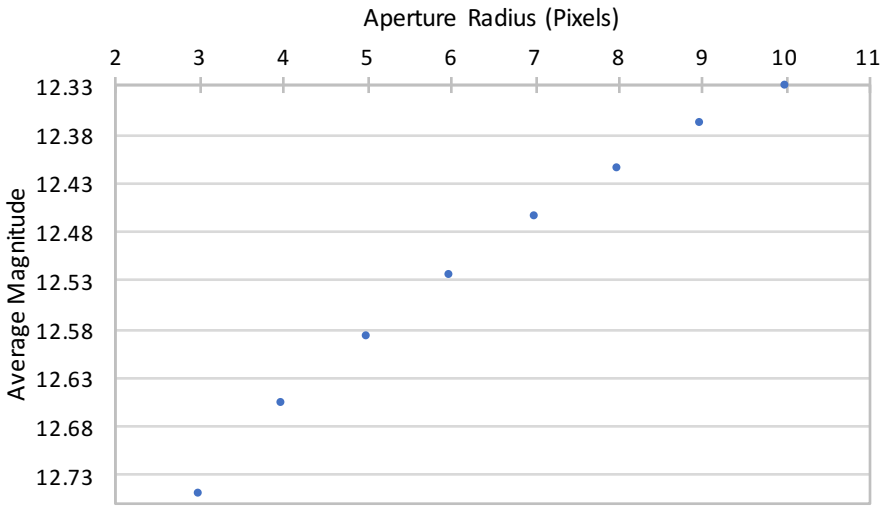

Figure 2.5 A plot of the average magnitude of NGC 4151 for each aperture radius. Notice that after an aperture radius of about six or seven pixels, the rate of change in magnitude begins to decrease. (Keep in mind that magnitude is a logarithmic scale.) This justifies the choice of an aperture radius of six pixels as the aperture radius that includes the entire object with minimal extra sky light.

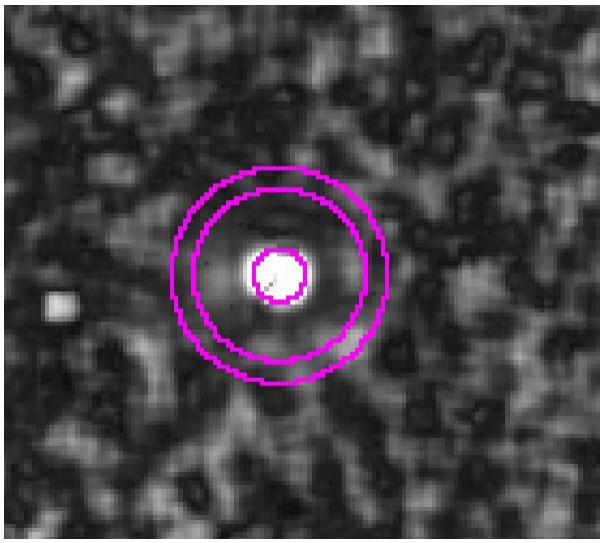

Figure 2.6 The subtracted image in the V filter (see Fig. 2.3) zoomed into the location of NGC 4151 to show that apertures. An inner radius of 20 pixels and an outer radius of 25 pixels were used for the sky annulus, and an aperture radius of 6 pixels was used for NGC 4151.

Table 2.2 Average standard magnitudes and errors (standard deviations) of the comparison stars in the B, V, R, and I filters. The standardization of these stars was part of a project completed by Dr. Joner (Joner 2017).

Star	B	err	V	err	R	err	I	err	B-V	err
C2	14.732	0.013	13.921	0.008	13.458	0.009	13.004	0.009	0.811	0.018
C3	14.010	0.008	12.790	0.007	12.142	0.004	11.545	0.014	1.220	0.011
C4	15.085	0.012	14.398	0.010	14.022	0.007	13.669	0.011	0.687	0.015
C5	13.230	0.011	12.580	0.006	12.215	0.006	11.866	0.007	0.650	0.013
av	14.264		13.422		12.959		12.521			

IRAF, AIJ, and ISIS are reported in Table 2.3. Note that the average differential magnitudes and errors of the comparison stars from IRAF were reported by Varstar, a script written by Dr. Hintz to assist in photometry with IRAF (Hintz 2015). The errors in this case are standard deviations. I found the differential magnitude of NGC 4151 from IRAF by finding the average of the differential magnitudes produced for each image by IRAF. I found the error for NGC 4151 from IRAF by finding the standard deviation of these differential magnitudes. AIJ reports the apparent magnitudes and error of NGC 4151 and the comparison stars for each image. Table 2.3 reports the average of these values. The errors in this case are based on photon statistics. After converting the ISIS relative flux units into magnitude (see Section 2.3.1), the average magnitude and error for NGC 4151 was found the same way as the IRAF average magnitude and error were found. The magnitudes and errors in the other filters can be found in Appendix A.

2.3.1 ISIS Flux to Magnitude Conversion

Because the units of flux produced by ISIS are unknown, converting to apparent magnitude is tricky. I used the method outlined in Székely et al. (2007). I began by finding the average,

Table 2.3 Average magnitudes and errors of NGC 4151 and the caparison stars in the V filter. Note that the average differential magnitudes and errors of the comparison stars from IRAF were reported by Varstar, a script written by Dr. Hintz to assist in photometry with IRAF (Hintz 2015). The errors in this case are standard deviations. I found the differential magnitude of NGC 4151 from IRAF by finding the average of the differential magnitudes produced for each image by IRAF. I found the error for NGC 4151 from IRAF by finding the standard deviation of these differential magnitudes. AIJ reports the apparent magnitudes and error of NGC 4151 and the comparison stars for each image. The table reports the average of these values. The errors in this case are based on photon statistics. After converting the ISIS relative flux units into magnitude (see Section 2.3.1), the average magnitude and error for NGC 4151 was found the same way as the IRAF average magnitude and error were found.

Object	IRAF av diff mag	err	AIJ av mag	av err	ISIS av mag	err
NGC 4151	-0.921	0.027	12.527	0.003	12.506	0.037
C2	0.463	0.008	13.921	0.004	...	...
C3	-0.593	0.010	12.790	0.002	...	...
C4	0.958	0.009	14.398	0.006	...	...
C5	-0.828	0.008	12.580	0.002	...	...

maximum, and minimum magnitudes of NGC 4151 produced using IRAF (m_{av}, m_{max}, and m_{min}, respectively), and the corresponding values produced by ISIS (F_{av}, F_{max}, and F_{min}, respectively). I then found the following values:

$$y_{\text{max}} = 10^{-0.4*(m_{\text{max}}-m_{\text{av}})}, \tag{2.2}$$

$$y_{\text{min}} = 10^{-0.4*(m_{\text{min}}-m_{\text{av}})}, \tag{2.3}$$

$$x_{\text{min}} = F_{\text{min}} - F_{\text{av}}, \tag{2.4}$$

and

$$x_{\text{max}} = F_{\text{max}} - F_{\text{av}}. \tag{2.5}$$

I then used the points $(x_{\text{min}}, y_{\text{min}})$ and $(x_{\text{max}}, y_{\text{max}})$ to find the slope, A, and the y-intercept, B. I used these values in the equation

$$m = \frac{\log A(F - F_{\text{av}}) + B}{0.4} + m_{\text{av}}, \tag{2.6}$$

where F is the flux produced by ISIS and m is the apparent magnitude that we are solving for. In summary, we are finding a linear equation to convert ISIS flux to magnitudes.

Chapter 3

Results, Conclusion, and Future

This chapter presents the light curves in the V filter and discusses the conclusions in Section 3.1. The possibilities of future work are discussed in Section 3.2.

3.1 Results and Conclusion

The overall shape of each light curve for NGC 4151 in the V filter produced with IRAF, AIJ, and ISIS is consistent for each of the methods, as can be seen in Fig. 3.1. However, there appears to be a great range of magnitudes and a greater amount of scatter in the light curve produced using ISIS. The apparent magnitudes produced using IRAF range from 12.434 mag to 12.568 mag, which is a difference of 0.134 mag. The apparent magnitudes produced using AIJ range from 12.265 mag to 12.595 mag, which is a difference of 0.129 mag. The apparent magnitudes produced using ISIS range from 12.416 mag to 12.599 mag, which is a difference of 0.183 mag. Thus AIJ and IRAF produce light curves with similar magnitude ranges, whereas ISIS produces a light curve with a greater range in apparent magnitudes.

To study the scatter of the light curves, fitted lines were found for the section of the light curves with a Geocentric Julian Date of 2457536.734 to a Geocentric Julian Date of 2457544.715. A

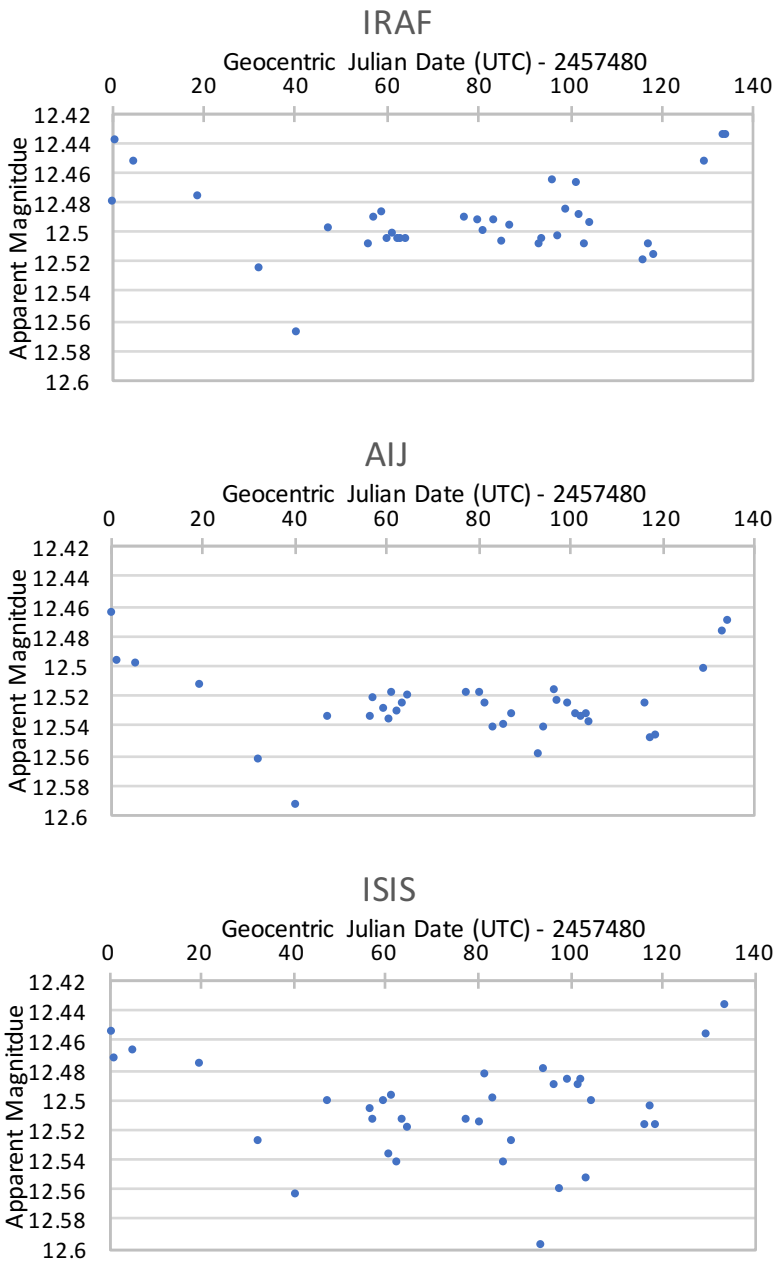

Figure 3.1 Light curves of NGC 4151 in the V filter using IRAF (top), AstroImageJ (middle), and ISIS (bottom). Notice that the overall shape of each curve is consistent for each process. However, some variations are present. In particular, the ISIS curve varies much more than the other curves.

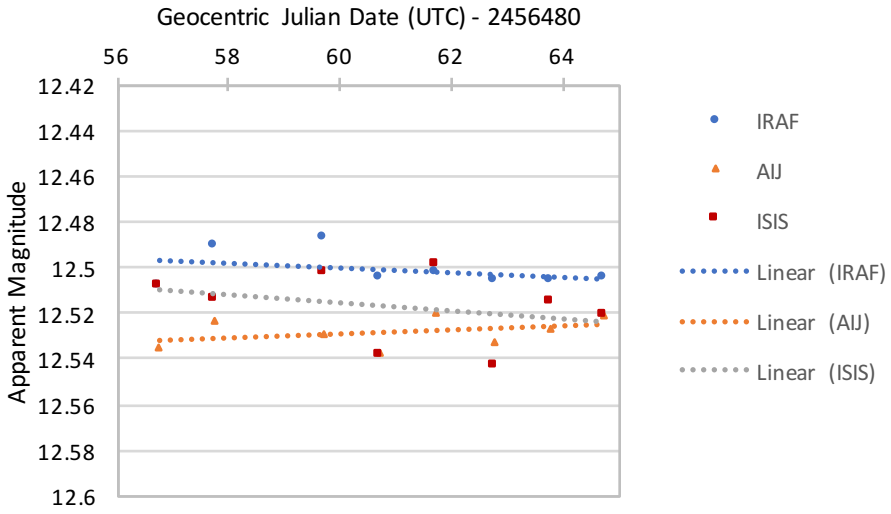

Figure 3.2 Plot of the light curves produced by IRAF, AIJ, and ISIS from Geocentric Julian Date 2457536.734 to Geocentric Julian Date 2457544.715. A fitted line for each method is produced using Excel. The equation of the fitted line for IRAF is $y = 0.001x + 12.441$, with an R^2 value of 0.135. The standard deviation of the line is 0.048. The equation of the fitted line for AIJ is $y = -0.0009x + 12.581$, with an R^2 value of 0.129. The standard deviation in the line is 0.042. The equation of the fitted line for ISIS is $y = 0.0018x + 12.407$, with an R^2 value of 0.100. The standard deviation in the line is 0.089.

plot of the data and fitted lines can be seen in Fig. 3.2. The equation of the fitted line for IRAF is $y = 0.001x + 12.441$, with a coefficient of determination, R^2, value of 0.135. The standard deviation of the line is 0.048. The equation of the fitted line for AIJ is $y = -0.0009x + 12.581$, with an R^2 value of 0.042. The standard deviation in the line is 0.245. The equation of the fitted line for ISIS is $y = 0.0018x + 12.407$, with an R^2 value of 0.100. The standard deviation in the line is 0.089. Thus, the fitted lines for this section of the light curves produced using IRAF and AIJ have similar R^2, as well as similar standard deviations. The fitted line for this section of the light curve produced by ISIS has the R^2 value closest to 1, as well as a standard deviation about twice that of the fitted lines for IRAF and AIJ. These values indicate that the light curve produced using ISIS has the most scatter.

This then begs the question. Is this scatter real, or is it a result of noise? If the scatter comes from noise, this then supports the use of differential aperture photometry over image subtraction photometry. On the other hand, if the scatter is real, this indicates that image subtraction photometry produces much more accurate results. The problem is that this is a difficult claim to prove. However, there are many sources of error in differential aperture photometry that are not issues for image subtraction photometry.

As discussed in Chapter 2, comparison stars must be chosen for aperture photometry. Which comparison stars are chosen can affect the results. For accurate results, the comparison stars should have about the same brightness as the the target and not be saturated. This is particularly difficult for galaxies because they tend to be rather bright. Thus, most stars in the field will either be dimmer than the target or saturated. This was a challenge for this particular field due to the lack of stars in the field. Furthermore, the comparison stars should have a constant light output. This is not always possible. Due to the limitations of available stars in this field, some of the comparison stars were not completely constant. An image subtraction technique eliminates this source of error completely because it does not use comparison stars.

Another advantage of using an image subtraction technique is that it eliminates the non-varying light from the rest of the galaxy, thus allowing one to measure the light from only the varying nucleus. The non-varying light from the galaxy can distort the light curve by smoothing it, making it appear to vary less than it actually does (see discussion on aperture size in Chapter 2). As can be seen in Figure 2.3 the light surrounding the nucleus of the galaxy, subtracts of very well. Thus, the light curve produced using ISIS should include light coming only from the nucleus. The greater range in the apparent magnitudes produced using ISIS, as well as the greater scatter, may be evidence that the light curves produced using IRAF and AIJ are smoothed due to domination from the non-varying light from the galaxy. Thus, results from ISIS could be more accurate than those from IRAF or AstroImageJ.

In conclusion, because ISIS eliminates many sources of error present in aperture photometry, it is reasonable to presume that, for this galaxies, image subtraction photometry is more accurate than differential aperture photometry. For AGN in general, ISIS is likely worthwhile due to the errors caused by the extra light from the surrounding galaxy. However, for distant galaxies, which appear as point sources, ISIS may not be worthwhile because the surrounding light cannot be subtracted off. Using the more accurate photometry technique is important because if image subtraction photometry yields more accurate time lags used in reverberation mapping, in would yield more accurate measurements of the mass of the super massive black hole at the center of the active galaxy. This thesis has shown that the light curves produced using image subtraction photometry differs from those using differential aperture photometry and is likely more accurate. Image subtraction photometry should therefore be used in reverberation mapping for this galaxy.

3.2 Further Work

Because this thesis looks at only one galaxy and three different methods, further work with other objects, and using other aperture and subtraction techniques, is necessary to verify the validity of these results.

Appendix A

Other Light Curves

The average and error tables, the subtracted image, and the light curves in filters B, I, R, and WA are presented. Note that due to the lack of standardized magnitudes in the WA filter, it was not possible to convert from differential magnitude to apparent magnitude. Additionally, due to problems with the images, the images for Geocentric Julian Dates: 2457576, 2457582, and 2457597 in the WA filter where left out.

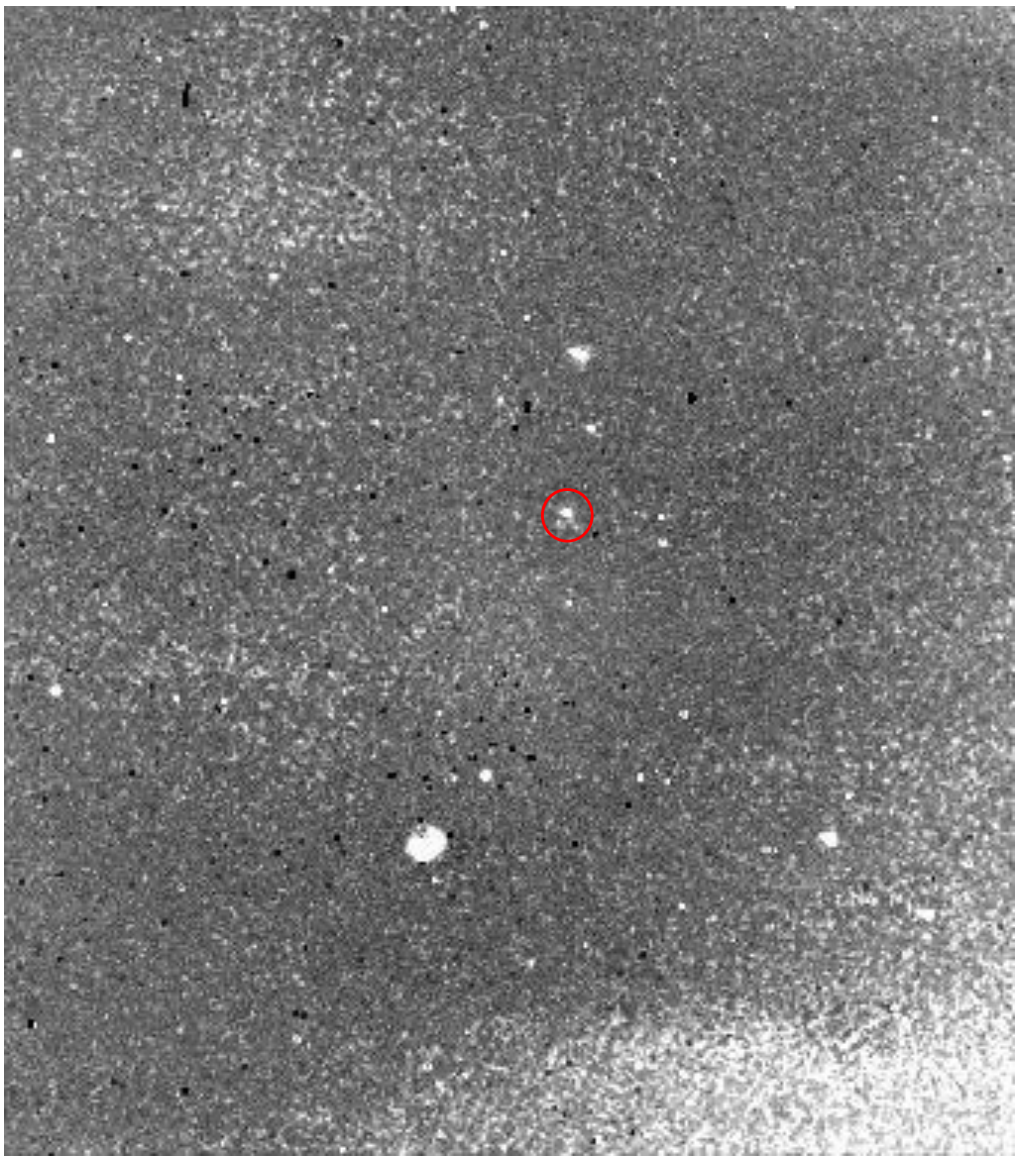

Figure A.1 The combined subtracted image in the B filter produced by ISIS. A subtracted frame is found for each image. The subtracted image is the original image with the constant light subtracted out. Thus, all that is left is the residual light, the light that is varying. The subtracted image is produced by adding the individual subtracted frames together. Thus the bright spots indicate the points of variation. As we can see, there is some noise in the frame. Additionally, there are a few bright spots produced by over-saturated stars. However, these do not affect our results for the galaxy. The location of the nucleus of the galaxy is indicated by the red circle. Notice the bright spot indicating a changing light flux.

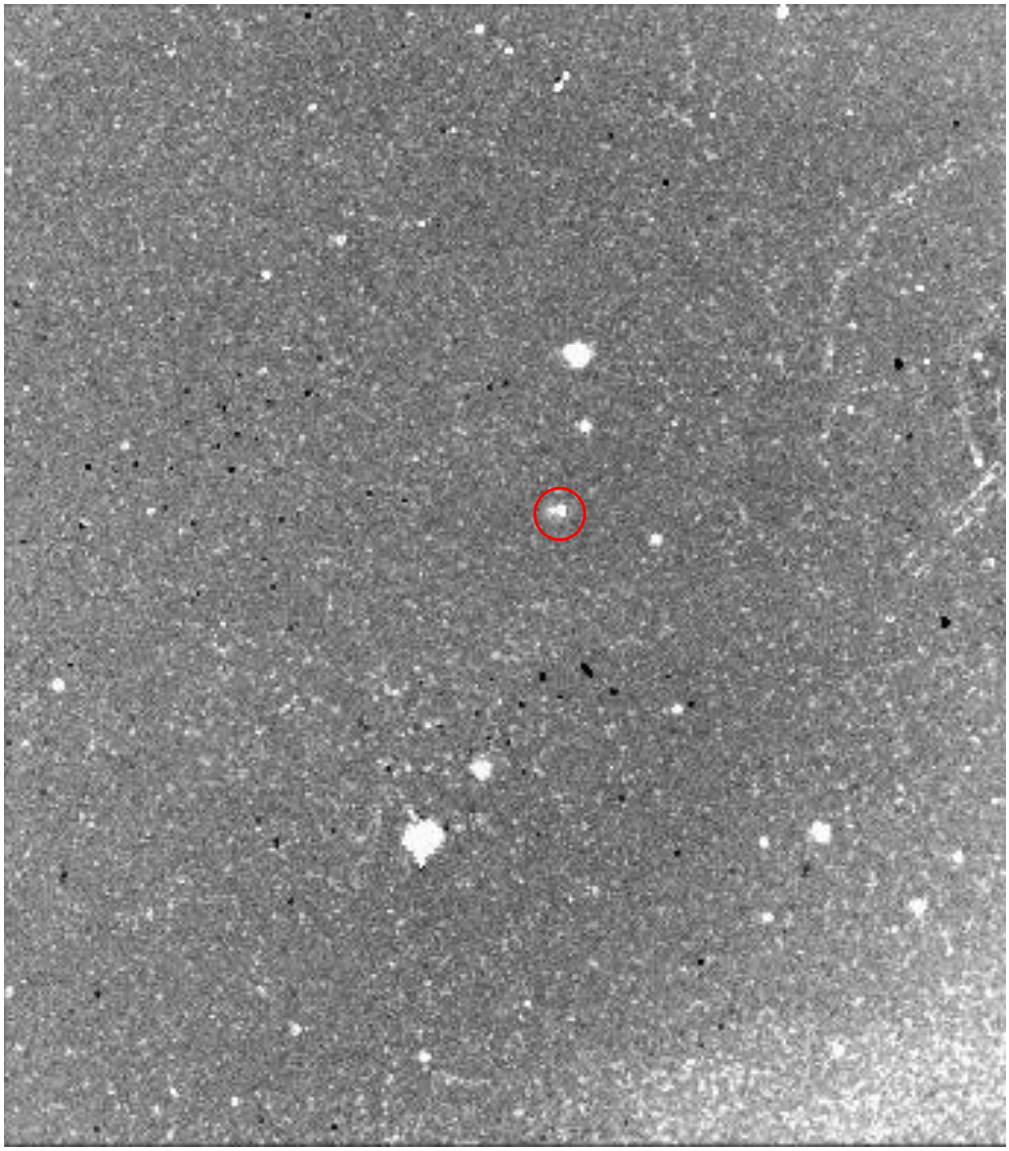

Figure A.2 The combined subtracted image in the R filter produced by ISIS.The bright spots indicate the points of variation. As we can see, there is some noise in the frame. Additionally, there are a few bright spots produced by over-saturated stars. However, these do not affect our results for the galaxy. The location of the nucleus of the galaxy is indicated by the red circle. Notice the bright spot indicating a changing light flux.

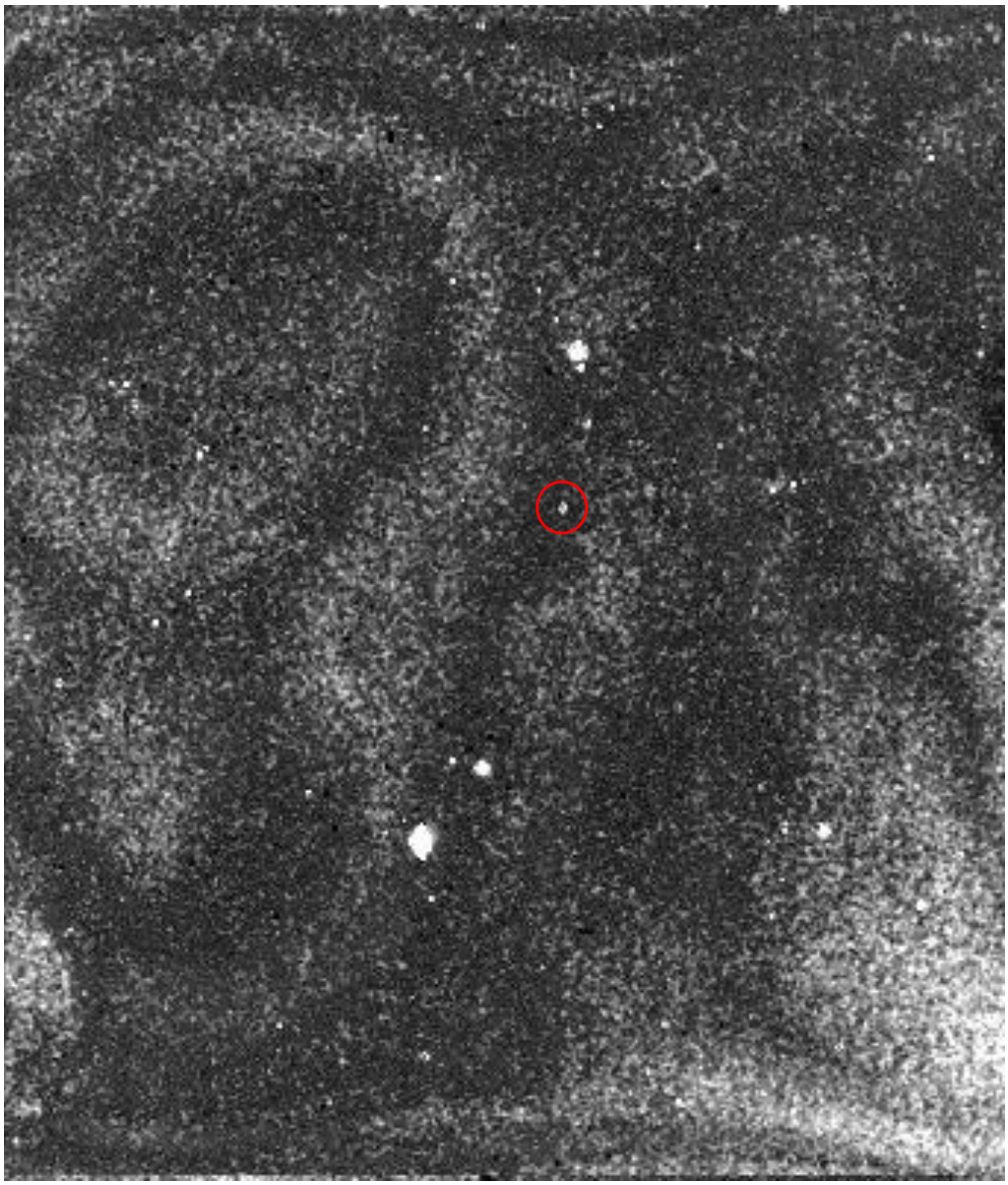

Figure A.3 The combined subtracted image in the I filter produced by ISIS. The bright spots indicate the points of variation. As we can see, there is some noise in the frame. Additionally, there are a few bright spots produced by over-saturated stars. However, these do not affect our results for the galaxy. The location of the nucleus of the galaxy is indicated by the red circle. Notice the bright spot indicating a changing light flux.

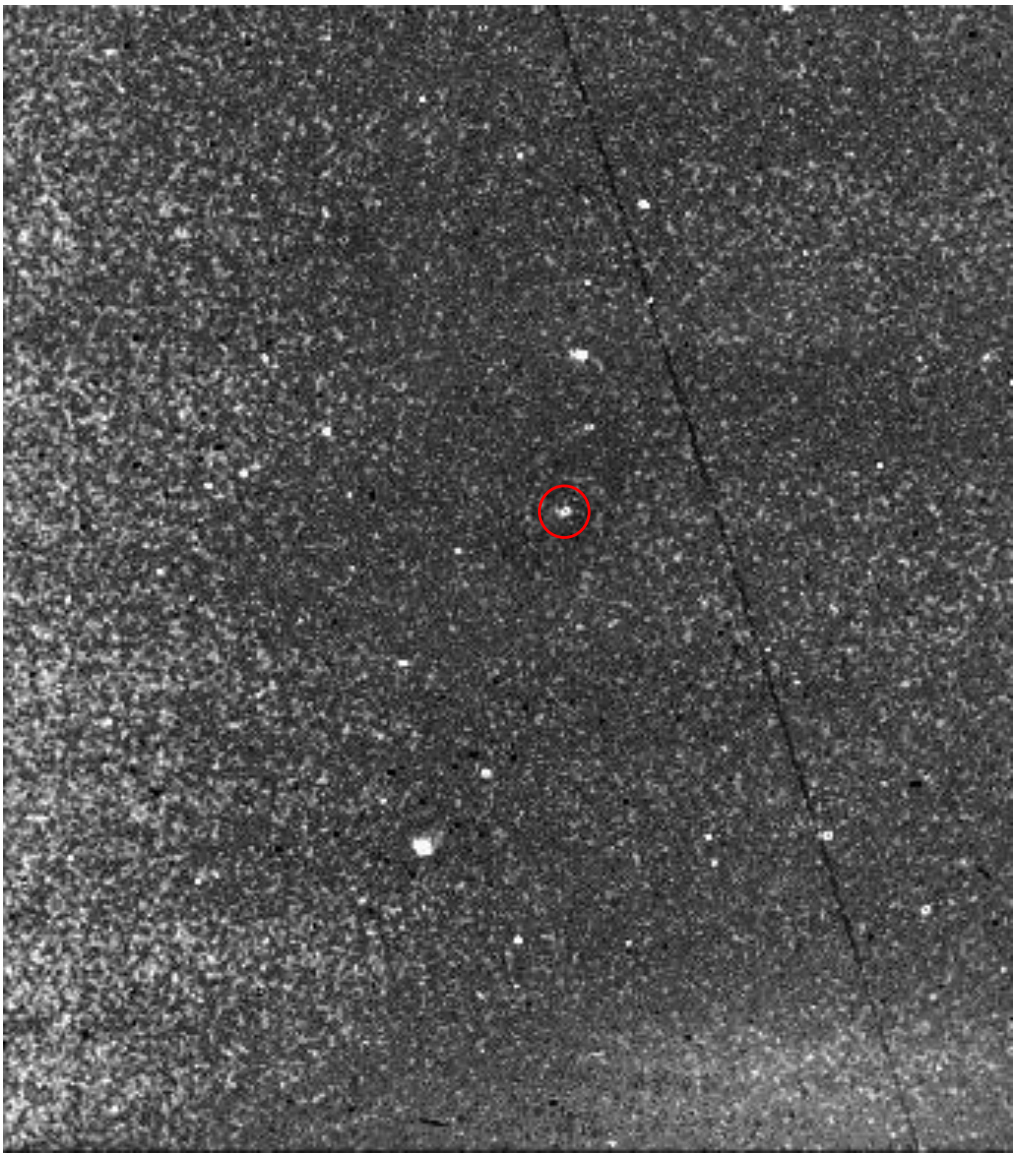

Figure A.4 The combined subtracted image in the WA filter produced by ISIS.The bright spots indicate the points of variation. As we can see, there is some noise in the frame. Additionally, there are a few bright spots produced by over-saturated stars. However, these do not affect our results for the galaxy. The location of the nucleus of the galaxy is indicated by the red circle. Notice the bright spot indicating a changing light flux.

Table A.1 Average magnitudes and errors of NGC 4151 and the caparison stars in the B filter. Note that the average differential magnitudes and errors of the comparison stars from IRAF were reported by Varstar, a script written by Dr. Hintz to assist in photometry with IRAF (Hintz 2015). The errors in this case are standard deviations. I found the differential magnitude of NGC 4151 from IRAF by finding the average of the differential magnitudes produced for each image by IRAF. I found the error for NGC 4151 from IRAF by finding the standard deviation of these differential magnitudes. AIJ reports the apparent magnitudes and error of NGC 4151 and the comparison stars for each image. The table reports the average of these values. The errors in this case are based on photon statistics. After converting the ISIS relative flux units into magnitude (see Section 2.3.1), the average magnitude and error for NGC 4151 was found the same way as the IRAF average magnitude and error were found.

Object	IRAF av diff mag	err	AIJ av mag	av err	ISIS av mag	err
NGC 4151	-1.048	0.040	13.253	0.003	13.192	0.051
C2	0.503	0.017	14.732	0.005	...	...
C3	-0.200	0.008	14.010	0.003	...	...
C4	0.769	0.016	15.085	0.006	...	...
C5	-1.072	0.006	13.230	0.002	...	...

Table A.2 Average magnitudes and errors of NGC 4151 and the caparison stars in the I filter. Note that the average differential magnitudes and errors of the comparison stars from IRAF were reported by Varstar, a script written by Dr. Hintz to assist in photometry with IRAF (Hintz 2015). The errors in this case are standard deviations. I found the differential magnitude of NGC 4151 from IRAF by finding the average of the differential magnitudes produced for each image by IRAF. I found the error for NGC 4151 from IRAF by finding the standard deviation of these differential magnitudes. AIJ reports the apparent magnitudes and error of NGC 4151 and the comparison stars for each image. The table reports the average of these values. The errors in this case are based on photon statistics. After converting the ISIS relative flux units into magnitude (see Section 2.3.1), the average magnitude and error for NGC 4151 was found the same way as the IRAF average magnitude and error were found.

Object	IRAF av diff mag	err	AIJ av mag	av err	ISIS av mag	err
NGC 4151	-0.672	0.023	11.840	0.002	11.904	0.054
C2	0.463	0.006	13.004	0.003	...	...
C3	-0.958	0.008	11.545	0.001	...	...
C4	1.149	0.007	13.669	0.004	...	...
C5	-1.654	0.012	11.866	0.002	...	...

Table A.3 Average magnitudes and errors of NGC 4151 and the caparison stars in the R filter. Note that the average differential magnitudes and errors of the comparison stars from IRAF were reported by Varstar, a script written by Dr. Hintz to assist in photometry with IRAF (Hintz 2015). The errors in this case are standard deviations. I found the differential magnitude of NGC 4151 from IRAF by finding the average of the differential magnitudes produced for each image by IRAF. I found the error for NGC 4151 from IRAF by finding the standard deviation of these differential magnitudes. AIJ reports the apparent magnitudes and error of NGC 4151 and the comparison stars for each image. The table reports the average of these values. The errors in this case are based on photon statistics. After converting the ISIS relative flux units into magnitude (see Section 2.3.1), the average magnitude and error for NGC 4151 was found the same way as the IRAF average magnitude and error were found.

Object	IRAF av diff mag	err	AIJ av mag	av err	ISIS av mag	err
NGC 4151	-0.971	0.031	12.004	0.018	11.904	0.054
C2	0.479	0.008	13.458	0.003	...	...
C3	-0.816	0.004	12.142	0.002	...	...
C4	1.072	0.006	14.002	0.004	...	...
C5	-0.735	0.006	12.215	0.002	...	...

Table A.4 Average differential magnitudes and errors of NGC 4151 and the caparison stars in the WA filter. Note that the average differential magnitudes and errors of the comparison stars from IRAF were reported by Varstar, a script written by Dr. Hintz to assist in photometry with IRAF (Hintz 2015). The errors in this case are standard deviations. I found the differential magnitude of NGC 4151 from IRAF by finding the average of the differential magnitudes produced for each image by IRAF. I found the error for NGC 4151 from IRAF by finding the standard deviation of these differential magnitudes. AIJ reports the differential flux and errors of NGC 4151 and the comparison stars for each image. The table reports the average of these values. Note that the av differential magnitudes reported for AIJ were converted from the av differential flux. The errors in this case are based on photon statistics. After converting the ISIS relative flux units into magnitude (see Section 2.3.1), the average differential magnitude and error for NGC 4151 was found the same way as the IRAF average differential magnitude and error were found.

Object	IRAF av diff mag	err	AIJ av diff mag	av err	ISIS av diff mag	err
NGC 4151	-2.040	0.033	-0.430	0.003	-2.035	0.095
C2	0.605	0.031	2.127	0.001	...	...
C3	-0.897	0.012	1.171	0.002	...	...
C4	1.017	0.011	-0.188	0.000	...	...
C5	-0.725	0.031	0.517	0.002	...	...

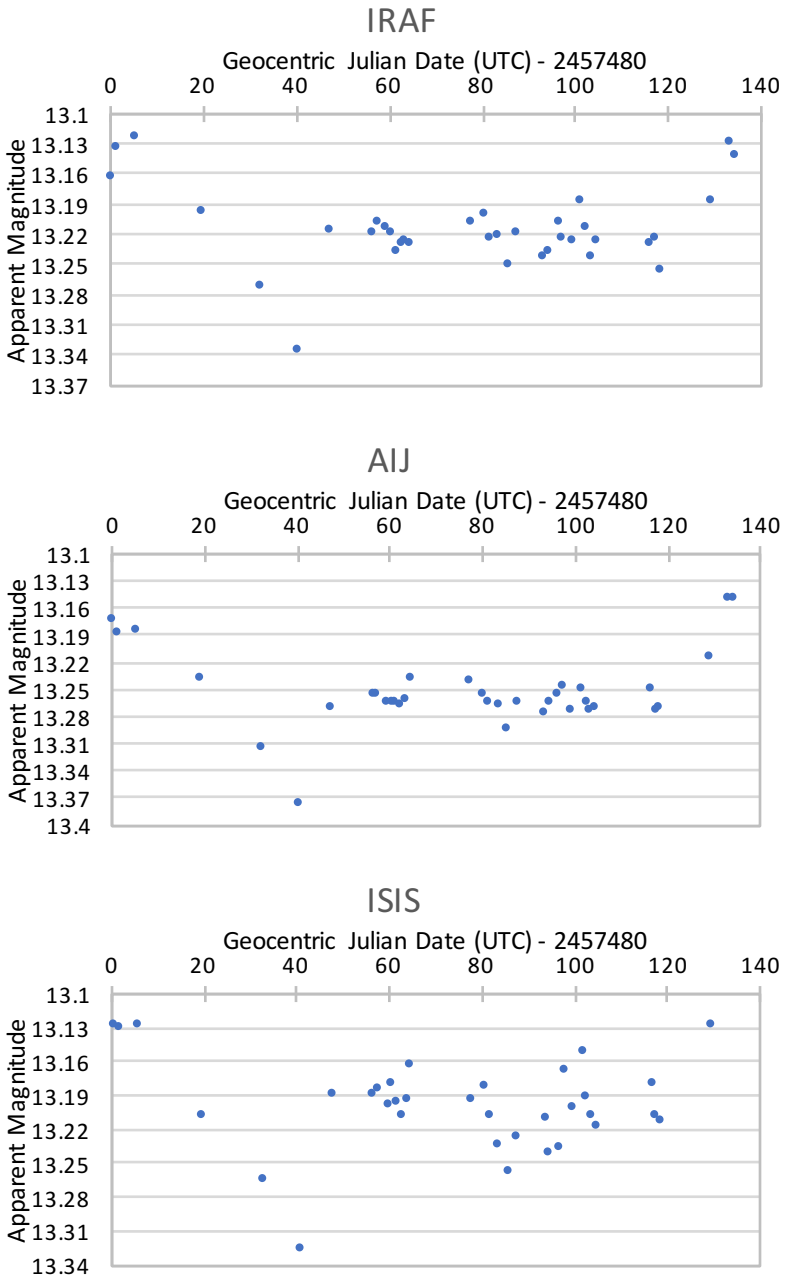

Figure A.5 Light curves of NGC 4151 in the B filter using IRAF (top), AstroImageJ (middle), and ISIS (bottom). Notice that the overall shape of each curve is consistent for each process. However, some variations are present. In particular, the ISIS curve varies much more than the other curves.

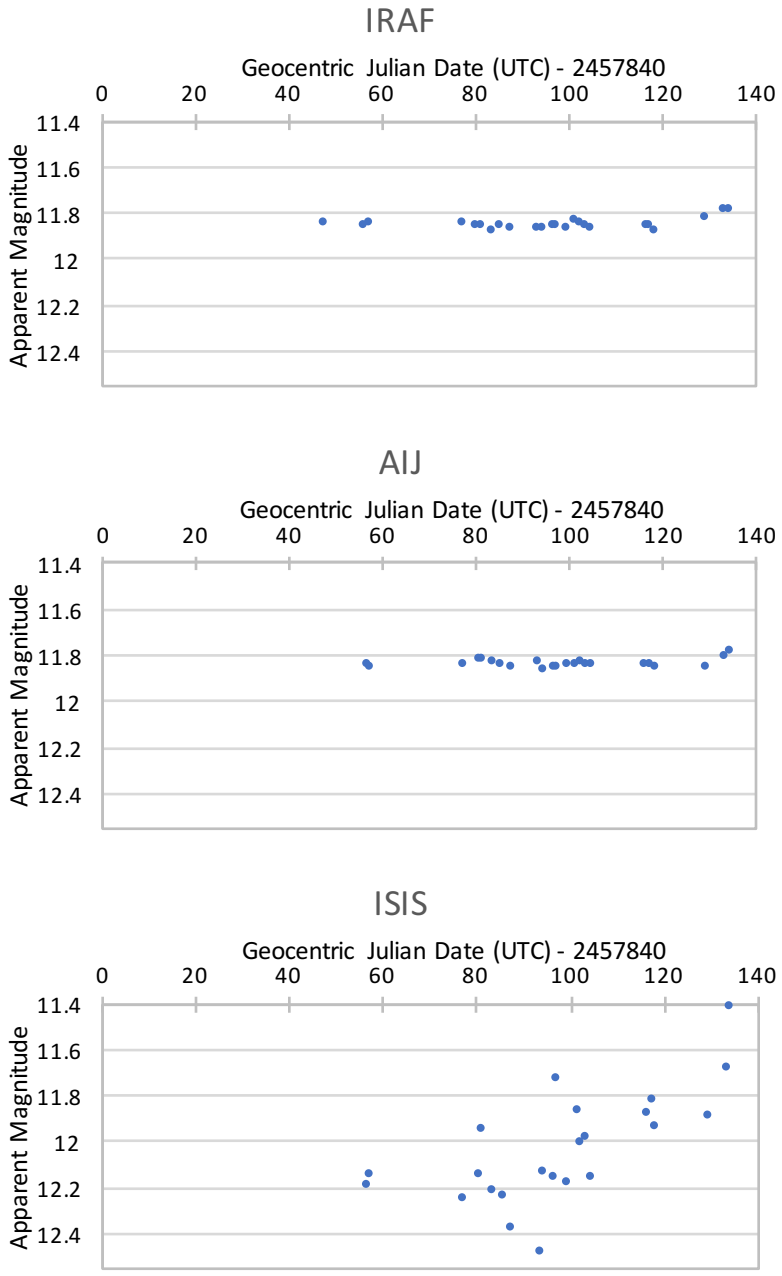

Figure A.6 Light curves of NGC 4151 in the I filter using IRAF (top), AstroImageJ (middle), and ISIS (bottom). Notice that the overall shape of each curve is consistent for each process. However, some variations are present. In particular, the ISIS curve varies much more than the other curves.

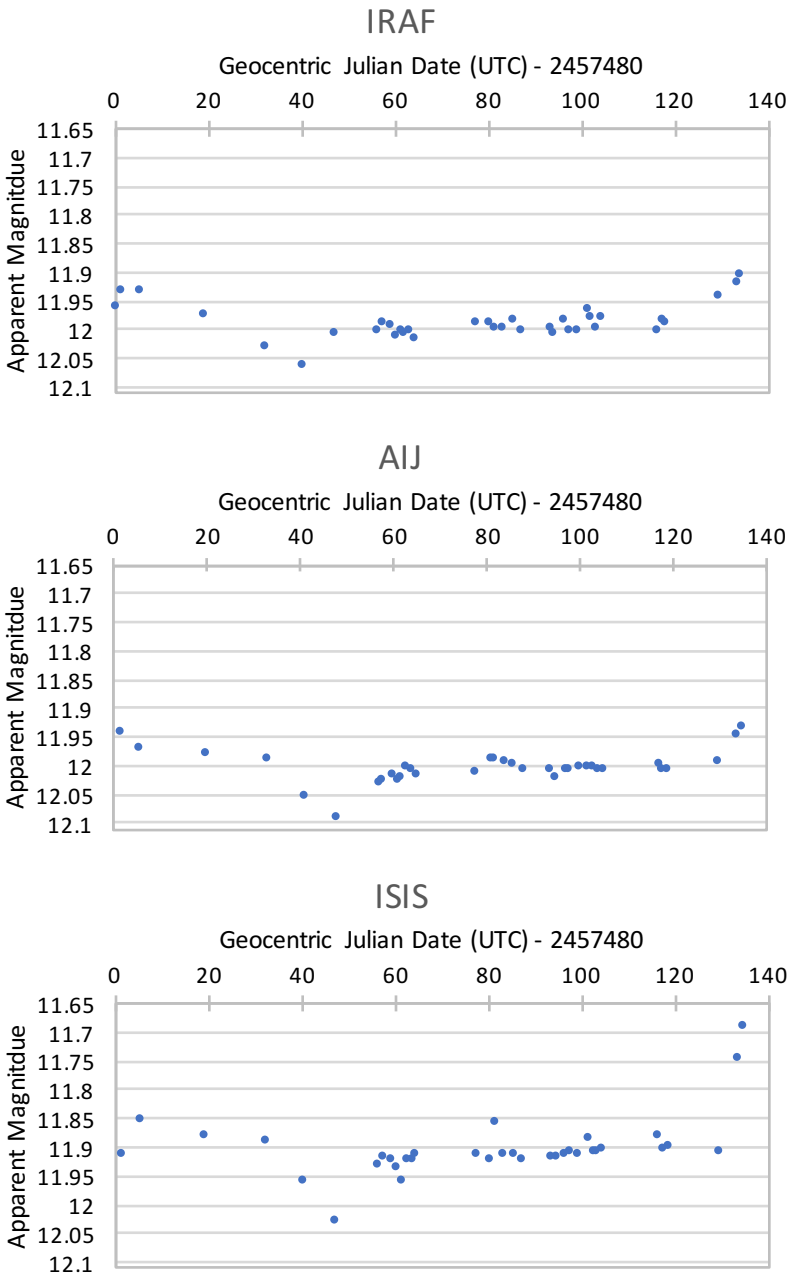

Figure A.7 Light curves of NGC 4151 in the R filter using IRAF (top), AstroImageJ (middle), and ISIS (bottom). Notice that the overall shape of each curve is consistent for each process. However, some variations are present. In particular, the ISIS curve varies much more than the other curves.

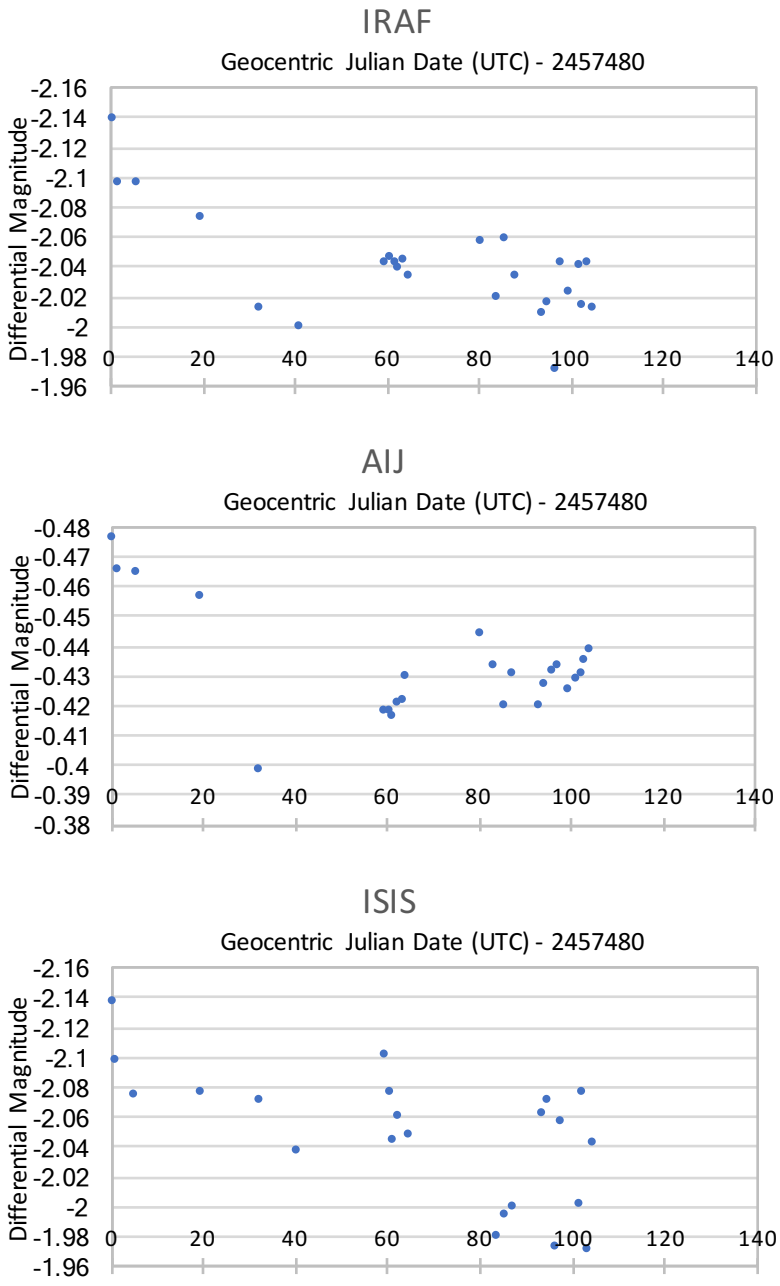

Figure A.8 Light curves of NGC 4151 in the WA filter using IRAF (top), AstroImageJ (middle), and ISIS (bottom). Notice that the overall shape of each curve is consistent for each process. However, some variations are present. In particular, the ISIS curve varies much more than the other curves.

Appendix B

Table of Observations

Table B.1 A summary of the observations of NGC 4151 carried out at the West Mountain Observatory.

Image Name	Date (mm/dd/yy)	HJD (+2457840)	Filter	Exposure Time (s)	Airmass
20160402_NGC4151-001B.fits	04/02/2016	0.6506	B	60	1.28
20160402_NGC4151-001R.fits	04/02/2016	0.6517	R	30	1.28
20160402_NGC4151-001V.fits	04/02/2016	0.6512	V	30	1.28
20160402_NGC4151-001WA.fits	04/02/2016	0.6524	WA	60	1.27
20160402_NGC4151-002B.fits	04/02/2016	0.6533	B	60	1.27
20160402_NGC4151-002R.fits	04/02/2016	0.6545	R	30	1.26
20160402_NGC4151-002V.fits	04/02/2016	0.6540	V	30	1.26
20160402_NGC4151-002WA.fits	04/02/2016	0.6551	WA	60	1.26
20160403_NGC4151-001B.fits	04/03/2016	1.6532	B	60	1.26
20160403_NGC4151-001R.fits	04/03/2016	1.6544	R	30	1.25
20160403_NGC4151-001V.fits	04/03/2016	1.6539	V	30	1.25

20160403_NGC4151-001WA.fits	04/03/2016	1.6551	WA	60	1.25
20160403_NGC4151-002B.fits	04/03/2016	1.6560	B	60	1.24
20160403_NGC4151-002R.fits	04/03/2016	1.6571	R	30	1.24
20160403_NGC4151-002V.fits	04/03/2016	1.6566	V	30	1.24
20160407_NGC4151-001B.fits	04/07/2016	5.6589	B	60	1.19
20160407_NGC4151-001R.fits	04/07/2016	5.6600	R	30	1.18
20160407_NGC4151-001WA.fits	04/07/2016	5.6607	WA	60	1.18
20160407_NGC4151-002B.fits	04/07/2016	5.6616	B	60	1.18
20160407_NGC4151-002R.fits	04/07/2016	5.6627	R	30	1.18
20160407_NGC4151-002V.fits	04/07/2016	5.6623	V	30	1.18
20160407_NGC4151-002WA.fits	04/07/2016	5.6634	WA	60	1.17
20160421_NGC4151-001B.fits	04/21/2016	19.6520	B	60	1.10
20160421_NGC4151-001R.fits	04/21/2016	19.6532	R	30	1.09
20160421_NGC4151-001V.fits	04/21/2016	19.6527	V	30	1.09
20160421_NGC4151-001WA.fits	04/21/2016	19.6538	WA	60	1.09
20160421_NGC4151-002B.fits	04/21/2016	19.6547	B	60	1.09
20160421_NGC4151-002R.fits	04/21/2016	19.6559	R	30	1.09
20160421_NGC4151-002V.fits	04/21/2016	19.6554	V	30	1.09
20160421_NGC4151-002WA.fits	04/21/2016	19.6566	WA	60	1.08
20160504_NGC4151-001B.fits	05/04/2016	32.6859	B	60	1.00
20160504_NGC4151-001R.fits	05/04/2016	32.6884	R	30	1.00
20160504_NGC4151-001V.fits	05/04/2016	32.6874	V	30	1.00
20160504_NGC4151-001WA.fits	05/04/2016	32.6895	WA	60	1.00
20160504_NGC4151-002B.fits	05/04/2016	32.6867	B	60	1.00
20160504_NGC4151-002R.fits	05/04/2016	32.6888	R	30	1.00

20160504_NGC4151-002V.fits	05/04/2016	32.6879	V	30	1.00
20160504_NGC4151-002WA.fits	05/04/2016	32.6903	WA	60	1.00
20160512_NGC4151-001B.fits	05/12/2016	40.8006	B	60	1.19
20160512_NGC4151-001R.fits	05/12/2016	40.8018	R	30	1.20
20160512_NGC4151-001V.fits	05/12/2016	40.8013	V	30	1.20
20160512_NGC4151-001WA.fits	05/12/2016	40.8025	WA	60	1.20
20160512_NGC4151-002B.fits	05/12/2016	40.8034	B	60	1.20
20160512_NGC4151-002R.fits	05/12/2016	40.8045	R	30	1.21
20160512_NGC4151-002V.fits	05/12/2016	40.8040	V	30	1.21
20160512_NGC4151-002WA.fits	05/12/2016	40.8052	WA	60	1.21
20160519_NGC4151-001B.fits	05/19/2016	47.6763	B	60	1.00
20160519_NGC4151-001I.fits	05/19/2016	47.6781	I	60	1.00
20160519_NGC4151-001R.fits	05/19/2016	47.6775	R	30	1.00
20160519_NGC4151-001V.fits	05/19/2016	47.6770	V	30	1.00
20160519_NGC4151-002B.fits	05/19/2016	47.6790	B	60	1.00
20160519_NGC4151-002I.fits	05/19/2016	47.6809	I	60	1.00
20160519_NGC4151-002R.fits	05/19/2016	47.6802	R	30	1.00
20160519_NGC4151-002V.fits	05/19/2016	47.6797	V	30	1.00
20160528_NGC4151-001B.fits	05/28/2016	56.7342	B	60	1.12
20160528_NGC4151-001I.fits	05/28/2016	56.7360	I	60	1.13
20160528_NGC4151-001R.fits	05/28/2016	56.7353	R	30	1.13
20160528_NGC4151-001V.fits	05/28/2016	56.7348	V	30	1.13
20160528_NGC4151-002B.fits	05/28/2016	56.7369	B	60	1.13
20160528_NGC4151-002I.fits	05/28/2016	56.7387	I	60	1.14
20160528_NGC4151-002R.fits	05/28/2016	56.7381	R	30	1.14

20160528_NGC4151-002V.fits	05/28/2016	56.7376	V	30	1.13
20160528_NGC4151-003B.fits	05/28/2016	56.7396	B	60	1.14
20160528_NGC4151-003I.fits	05/28/2016	56.7415	I	60	1.15
20160528_NGC4151-003R.fits	05/28/2016	56.7408	R	30	1.14
20160528_NGC4151-003V.fits	05/28/2016	56.7403	V	30	1.14
20160529_NGC4151-001B.fits	05/29/2016	57.7267	B	60	1.11
20160529_NGC4151-001I.fits	05/29/2016	57.7285	I	60	1.12
20160529_NGC4151-001R.fits	05/29/2016	57.7278	R	30	1.12
20160529_NGC4151-001V.fits	05/29/2016	57.7273	V	30	1.11
20160529_NGC4151-002B.fits	05/29/2016	57.7294	B	60	1.12
20160529_NGC4151-002I.fits	05/29/2016	57.7312	I	60	1.12
20160529_NGC4151-002R.fits	05/29/2016	57.7306	R	30	1.12
20160529_NGC4151-002V.fits	05/29/2016	57.7301	V	30	1.12
20160529_NGC4151-003B.fits	05/29/2016	57.7321	B	60	1.13
20160529_NGC4151-003I.fits	05/29/2016	57.7340	I	60	1.13
20160529_NGC4151-003R.fits	05/29/2016	57.7333	R	30	1.13
20160529_NGC4151-003V.fits	05/29/2016	57.7328	V	30	1.13
20160531_NGC4151-001B.fits	05/31/2016	59.6778	B	60	1.03
20160531_NGC4151-001R.fits	05/31/2016	59.6790	R	30	1.03
20160531_NGC4151-001V.fits	05/31/2016	59.6785	V	30	1.03
20160531_NGC4151-001WA.fits	05/31/2016	59.6798	WA	60	1.03
20160531_NGC4151-002B.fits	05/31/2016	59.6808	B	60	1.03
20160531_NGC4151-002R.fits	05/31/2016	59.6820	R	30	1.04
20160531_NGC4151-002V.fits	05/31/2016	59.6815	V	30	1.04
20160531_NGC4151-002WA.fits	05/31/2016	59.6828	WA	60	1.04

20160601_NGC4151-001B.fits	06/01/2016	60.7119	B	60	1.10
20160601_NGC4151-001R.fits	06/01/2016	60.7143	R	30	1.10
20160601_NGC4151-001V.fits	06/01/2016	60.7134	V	30	1.10
20160601_NGC4151-001WA.fits	06/01/2016	60.7155	WA	60	1.11
20160601_NGC4151-002B.fits	06/01/2016	60.7127	B	60	1.10
20160601_NGC4151-002R.fits	06/01/2016	60.7148	R	30	1.10
20160601_NGC4151-002V.fits	06/01/2016	60.7138	V	30	1.10
20160601_NGC4151-002WA.fits	06/01/2016	60.7163	WA	60	1.11
20160602_NGC4151-001B.fits	06/02/2016	61.7273	B	60	1.15
20160602_NGC4151-001R.fits	06/02/2016	61.7284	R	30	1.15
20160602_NGC4151-001V.fits	06/02/2016	61.7279	V	30	1.15
20160602_NGC4151-001WA.fits	06/02/2016	61.7291	WA	60	1.15
20160602_NGC4151-002B.fits	06/02/2016	61.7300	B	60	1.15
20160602_NGC4151-002R.fits	06/02/2016	61.7312	R	30	1.16
20160602_NGC4151-002V.fits	06/02/2016	61.7307	V	30	1.16
20160602_NGC4151-002WA.fits	06/02/2016	61.7318	WA	60	1.16
20160603_NGC4151-001B.fits	06/03/2016	62.7418	B	60	1.20
20160603_NGC4151-001R.fits	06/03/2016	62.7429	R	30	1.21
20160603_NGC4151-001V.fits	06/03/2016	62.7424	V	30	1.21
20160603_NGC4151-001WA.fits	06/03/2016	62.7436	WA	60	1.21
20160603_NGC4151-002B.fits	06/03/2016	62.7445	B	60	1.21
20160603_NGC4151-002R.fits	06/03/2016	62.7457	R	30	1.22
20160603_NGC4151-002V.fits	06/03/2016	62.7452	V	30	1.22
20160603_NGC4151-002WA.fits	06/03/2016	62.7463	WA	60	1.22
20160604_NGC4151-001B.fits	06/04/2016	63.7679	B	60	1.34

20160604_NGC4151-001R.fits	06/04/2016	63.7706	R	30	1.35
20160604_NGC4151-001V.fits	06/04/2016	63.7695	V	30	1.34
20160604_NGC4151-001WA.fits	06/04/2016	63.7719	WA	60	1.36
20160604_NGC4151-002B.fits	06/04/2016	63.7688	B	60	1.34
20160604_NGC4151-002R.fits	06/04/2016	63.7712	R	30	1.35
20160604_NGC4151-002V.fits	06/04/2016	63.7701	V	30	1.35
20160604_NGC4151-002WA.fits	06/04/2016	63.7728	WA	60	1.36
20160605_NGC4151-001B.fits	06/05/2016	64.7146	B	60	1.13
20160605_NGC4151-001R.fits	06/05/2016	64.7157	R	30	1.14
20160605_NGC4151-001V.fits	06/05/2016	64.7152	V	30	1.13
20160605_NGC4151-001WA.fits	06/05/2016	64.7164	WA	60	1.14
20160605_NGC4151-002B.fits	06/05/2016	64.7173	B	60	1.14
20160605_NGC4151-002R.fits	06/05/2016	64.7185	R	30	1.14
20160605_NGC4151-002V.fits	06/05/2016	64.7180	V	30	1.14
20160605_NGC4151-002WA.fits	06/05/2016	64.7191	WA	60	1.15
20160618_NGC4151-001B.fits	06/18/2016	77.6949	B	120	1.19
20160618_NGC4151-001I.fits	06/18/2016	77.6989	I	100	1.20
20160618_NGC4151-001R.fits	06/18/2016	77.6976	R	100	1.20
20160618_NGC4151-001V.fits	06/18/2016	77.6963	V	100	1.19
20160618_NGC4151-002B.fits	06/18/2016	77.7014	B	120	1.21
20160618_NGC4151-002I.fits	06/18/2016	77.7054	I	100	1.23
20160618_NGC4151-002R.fits	06/18/2016	77.7041	R	100	1.22
20160618_NGC4151-002V.fits	06/18/2016	77.7028	V	100	1.22
20160621_NGC4151-001B.fits	06/21/2016	80.6849	B	120	1.18
20160621_NGC4151-001I.fits	06/21/2016	80.6889	I	100	1.20

20160621_NGC4151-001R.fits	06/21/2016	80.6876	R	100	1.19
20160621_NGC4151-001V.fits	06/21/2016	80.6863	V	100	1.19
20160621_NGC4151-001WA.fits	06/21/2016	80.6902	WA	100	1.20
20160621_NGC4151-002B.fits	06/21/2016	80.6917	B	120	1.21
20160621_NGC4151-002I.fits	06/21/2016	80.6957	I	100	1.22
20160621_NGC4151-002R.fits	06/21/2016	80.6944	R	100	1.22
20160621_NGC4151-002V.fits	06/21/2016	80.6931	V	100	1.21
20160621_NGC4151-002WA.fits	06/21/2016	80.6970	WA	100	1.23
20160622_NGC4151-001B.fits	06/22/2016	81.6810	B	120	1.18
20160622_NGC4151-001I.fits	06/22/2016	81.6850	I	100	1.19
20160622_NGC4151-001R.fits	06/22/2016	81.6837	R	100	1.19
20160622_NGC4151-001V.fits	06/22/2016	81.6824	V	100	1.18
20160622_NGC4151-002B.fits	06/22/2016	81.6865	B	120	1.20
20160622_NGC4151-002I.fits	06/22/2016	81.6905	I	100	1.21
20160622_NGC4151-002R.fits	06/22/2016	81.6892	R	100	1.21
20160624_NGC4151-001B.fits	06/24/2016	83.7133	B	120	1.34
20160624_NGC4151-001I.fits	06/24/2016	83.7091	I	100	1.32
20160624_NGC4151-001R.fits	06/24/2016	83.7118	R	100	1.34
20160624_NGC4151-001V.fits	06/24/2016	83.7105	V	100	1.33
20160624_NGC4151-001WA.fits	06/24/2016	83.7145	WA	60	1.35
20160624_NGC4151-002B.fits	06/24/2016	83.7219	B	120	1.39
20160624_NGC4151-002R.fits	06/24/2016	83.7204	R	100	1.38
20160624_NGC4151-002V.fits	06/24/2016	83.7190	V	100	1.38
20160624_NGC4151-002WA.fits	06/24/2016	83.7231	WA	60	1.40
20160626_NGC4151-001B.fits	06/26/2016	85.7061	B	120	1.34

20160626_NGC4151-001R.fits	06/26/2016	85.7046	R	100	1.33
20160626_NGC4151-001V.fits	06/26/2016	85.7033	V	100	1.32
20160626_NGC4151-001WA.fits	06/26/2016	85.7075	WA	100	1.34
20160626_NGC4151-002B.fits	06/26/2016	85.7131	B	120	1.38
20160626_NGC4151-002I.fits	06/26/2016	85.7089	I	100	1.35
20160626_NGC4151-002R.fits	06/26/2016	85.7116	R	100	1.37
20160626_NGC4151-002V.fits	06/26/2016	85.7103	V	100	1.36
20160626_NGC4151-002WA.fits	06/26/2016	85.7146	WA	100	1.38
20160628_NGC4151-001B.fits	06/28/2016	87.7051	B	120	1.36
20160628_NGC4151-001I.fits	06/28/2016	87.7009	I	100	1.34
20160628_NGC4151-001R.fits	06/28/2016	87.7036	R	100	1.35
20160628_NGC4151-001V.fits	06/28/2016	87.7023	V	100	1.35
20160628_NGC4151-001WA.fits	06/28/2016	87.7065	WA	100	1.37
20160628_NGC4151-002B.fits	06/28/2016	87.7131	B	120	1.41
20160628_NGC4151-002I.fits	06/28/2016	87.7089	I	100	1.38
20160628_NGC4151-002R.fits	06/28/2016	87.7116	R	100	1.40
20160628_NGC4151-002V.fits	06/28/2016	87.7103	V	100	1.39
20160628_NGC4151-002WA.fits	06/28/2016	87.7146	WA	100	1.42
20160704_NGC4151-001B.fits	07/04/2016	93.6885	B	120	1.36
20160704_NGC4151-001I.fits	07/04/2016	93.6925	I	100	1.39
20160704_NGC4151-001R.fits	07/04/2016	93.6913	R	100	1.38
20160704_NGC4151-001V.fits	07/04/2016	93.6899	V	100	1.37
20160704_NGC4151-001WA.fits	07/04/2016	93.6938	WA	100	1.39
20160704_NGC4151-002B.fits	07/04/2016	93.6953	B	120	1.40
20160704_NGC4151-002I.fits	07/04/2016	93.6993	I	100	1.43

20160704_NGC4151-002R.fits	07/04/2016	93.6980	R	100	1.42
20160704_NGC4151-002V.fits	07/04/2016	93.6967	V	100	1.41
20160704_NGC4151-002WA.fits	07/04/2016	93.7006	WA	100	1.44
20160705_NGC4151-001B.fits	07/05/2016	94.6914	B	120	1.40
20160705_NGC4151-001I.fits	07/05/2016	94.6954	I	100	1.42
20160705_NGC4151-001R.fits	07/05/2016	94.6941	R	100	1.41
20160705_NGC4151-001V.fits	07/05/2016	94.6928	V	100	1.41
20160705_NGC4151-001WA.fits	07/05/2016	94.6967	WA	100	1.43
20160705_NGC4151-002B.fits	07/05/2016	94.6982	B	120	1.44
20160705_NGC4151-002I.fits	07/05/2016	94.7022	I	100	1.47
20160705_NGC4151-002R.fits	07/05/2016	94.7009	R	100	1.46
20160705_NGC4151-002WA.fits	07/05/2016	94.7035	WA	100	1.48
20160707_NGC4151-001B.fits	07/07/2016	96.6959	B	60	1.46
20160707_NGC4151-001I.fits	07/07/2016	96.6978	I	45	1.48
20160707_NGC4151-001R.fits	07/07/2016	96.6972	R	30	1.47
20160707_NGC4151-001V.fits	07/07/2016	96.6967	V	45	1.47
20160707_NGC4151-001WA.fits	07/07/2016	96.6986	WA	60	1.48
20160707_NGC4151-002B.fits	07/07/2016	96.6995	B	60	1.49
20160707_NGC4151-002V.fits	07/07/2016	96.7002	V	45	1.49
20160707_NGC4151-002WA.fits	07/07/2016	96.7021	WA	60	1.51
20160708_NGC4151-001B.fits	07/08/2016	97.6780	B	60	1.37
20160708_NGC4151-001I.fits	07/08/2016	97.6799	I	45	1.38
20160708_NGC4151-001R.fits	07/08/2016	97.6793	R	30	1.37
20160708_NGC4151-001V.fits	07/08/2016	97.6788	V	45	1.37
20160708_NGC4151-001WA.fits	07/08/2016	97.6807	WA	60	1.38

20160708_NGC4151-002B.fits	07/08/2016	97.6824	B	60	1.39
20160708_NGC4151-002I.fits	07/08/2016	97.6843	I	45	1.40
20160708_NGC4151-002R.fits	07/08/2016	97.6837	R	30	1.40
20160708_NGC4151-002V.fits	07/08/2016	97.6815	V	45	1.39
20160708_NGC4151-002WA.fits	07/08/2016	97.6850	WA	60	1.41
20160708_NGC4151-003V.fits	07/08/2016	97.6831	V	45	1.40
20160710_NGC4151-001B.fits	07/10/2016	99.6990	B	70	1.55
20160710_NGC4151-001I.fits	07/10/2016	99.7009	I	45	1.57
20160710_NGC4151-001R.fits	07/10/2016	99.7004	R	30	1.56
20160710_NGC4151-001V.fits	07/10/2016	99.6998	V	45	1.56
20160710_NGC4151-001WA.fits	07/10/2016	99.7017	WA	60	1.57
20160710_NGC4151-002B.fits	07/10/2016	99.7027	B	70	1.58
20160710_NGC4151-002I.fits	07/10/2016	99.7046	I	45	1.60
20160710_NGC4151-002R.fits	07/10/2016	99.7040	R	30	1.59
20160710_NGC4151-002V.fits	07/10/2016	99.7035	V	45	1.59
20160710_NGC4151-002WA.fits	07/10/2016	99.7054	WA	60	1.61
20160712_NGC4151-001B.fits	07/12/2016	101.6982	B	60	1.59
20160712_NGC4151-001I.fits	07/12/2016	101.7001	I	45	1.61
20160712_NGC4151-001R.fits	07/12/2016	101.6995	R	30	1.60
20160712_NGC4151-001V.fits	07/12/2016	101.6989	V	45	1.60
20160712_NGC4151-001WA.fits	07/12/2016	101.7008	WA	60	1.61
20160712_NGC4151-002B.fits	07/12/2016	101.7017	B	60	1.62
20160712_NGC4151-002I.fits	07/12/2016	101.7036	I	45	1.64
20160712_NGC4151-002R.fits	07/12/2016	101.7031	R	30	1.64
20160712_NGC4151-002V.fits	07/12/2016	101.7025	V	45	1.63

20160712_NGC4151-002WA.fits	07/12/2016	101.7044	WA	60	1.65
20160713_NGC4151-001B.fits	07/13/2016	102.6885	B	60	1.53
20160713_NGC4151-001I.fits	07/13/2016	102.6904	I	45	1.55
20160713_NGC4151-001R.fits	07/13/2016	102.6899	R	30	1.54
20160713_NGC4151-001V.fits	07/13/2016	102.6893	V	45	1.54
20160713_NGC4151-001WA.fits	07/13/2016	102.6912	WA	60	1.56
20160713_NGC4151-002B.fits	07/13/2016	102.6921	B	60	1.56
20160713_NGC4151-002I.fits	07/13/2016	102.6940	I	45	1.58
20160713_NGC4151-002R.fits	07/13/2016	102.6934	R	30	1.57
20160713_NGC4151-002V.fits	07/13/2016	102.6929	V	45	1.57
20160713_NGC4151-002WA.fits	07/13/2016	102.6948	WA	60	1.59
20160714_NGC4151-001B.fits	07/14/2016	103.6678	B	60	1.41
20160714_NGC4151-001I.fits	07/14/2016	103.6697	I	45	1.42
20160714_NGC4151-001R.fits	07/14/2016	103.6692	R	30	1.41
20160714_NGC4151-001V.fits	07/14/2016	103.6686	V	45	1.41
20160714_NGC4151-001WA.fits	07/14/2016	103.6708	WA	120	1.43
20160714_NGC4151-002B.fits	07/14/2016	103.6721	B	60	1.43
20160714_NGC4151-002I.fits	07/14/2016	103.6740	I	45	1.45
20160714_NGC4151-002R.fits	07/14/2016	103.6734	R	30	1.44
20160714_NGC4151-002V.fits	07/14/2016	103.6728	V	45	1.44
20160714_NGC4151-002WA.fits	07/14/2016	103.6751	WA	120	1.45
20160715_NGC4151-001B.fits	07/15/2016	104.6832	B	60	1.54
20160715_NGC4151-001I.fits	07/15/2016	104.6851	I	45	1.55
20160715_NGC4151-001R.fits	07/15/2016	104.6845	R	30	1.55
20160715_NGC4151-001V.fits	07/15/2016	104.6839	V	45	1.54

20160715_NGC4151-001WA.fits	07/15/2016	104.6899	WA	60	1.59
20160715_NGC4151-002B.fits	07/15/2016	104.6859	B	60	1.56
20160715_NGC4151-002I.fits	07/15/2016	104.6878	I	45	1.57
20160715_NGC4151-002R.fits	07/15/2016	104.6872	R	30	1.57
20160715_NGC4151-002V.fits	07/15/2016	104.6867	V	45	1.56
20160715_NGC4151-002WA.fits	07/15/2016	104.6907	WA	60	1.60
20160727_NGC4151-001B.fits	07/27/2016	116.6713	B	60	1.74
20160727_NGC4151-001I.fits	07/27/2016	116.6732	I	45	1.76
20160727_NGC4151-001R.fits	07/27/2016	116.6727	R	30	1.75
20160727_NGC4151-001V.fits	07/27/2016	116.6721	V	45	1.74
20160727_NGC4151-001WA.fits	07/27/2016	116.6740	WA	60	1.77
20160727_NGC4151-002B.fits	07/27/2016	116.6749	B	60	1.78
20160727_NGC4151-002I.fits	07/27/2016	116.6768	I	45	1.80
20160727_NGC4151-002R.fits	07/27/2016	116.6762	R	30	1.79
20160727_NGC4151-002V.fits	07/27/2016	116.6756	V	45	1.78
20160727_NGC4151-002WA.fits	07/27/2016	116.6776	WA	60	1.81
20160728_NGC4151-001B.fits	07/28/2016	117.6681	B	60	1.73
20160728_NGC4151-001I.fits	07/28/2016	117.6700	I	45	1.75
20160728_NGC4151-001R.fits	07/28/2016	117.6694	R	30	1.75
20160728_NGC4151-001V.fits	07/28/2016	117.6688	V	45	1.74
20160728_NGC4151-001WA.fits	07/28/2016	117.6707	WA	60	1.76
20160728_NGC4151-002B.fits	07/28/2016	117.6716	B	60	1.77
20160728_NGC4151-002I.fits	07/28/2016	117.6736	I	45	1.79
20160728_NGC4151-002R.fits	07/28/2016	117.6730	R	30	1.79
20160728_NGC4151-002V.fits	07/28/2016	117.6724	V	45	1.78

20160728_NGC4151-002WA.fits	07/28/2016	117.6743	WA	60	1.80
20160729_NGC4151-001B.fits	07/29/2016	118.6709	B	60	1.79
20160729_NGC4151-001I.fits	07/29/2016	118.6728	I	45	1.82
20160729_NGC4151-001R.fits	07/29/2016	118.6723	R	30	1.81
20160729_NGC4151-001V.fits	07/29/2016	118.6717	V	45	1.80
20160729_NGC4151-001WA.fits	07/29/2016	118.6736	WA	60	1.83
20160729_NGC4151-002B.fits	07/29/2016	118.6745	B	60	1.84
20160729_NGC4151-002I.fits	07/29/2016	118.6764	I	45	1.86
20160729_NGC4151-002R.fits	07/29/2016	118.6758	R	30	1.85
20160729_NGC4151-002V.fits	07/29/2016	118.6753	V	45	1.85
20160729_NGC4151-002WA.fits	07/29/2016	118.6772	WA	60	1.87
20160809_NGC4151-001B.fits	08/09/2016	129.6588	B	60	2.04
20160809_NGC4151-001I.fits	08/09/2016	129.6627	I	45	2.10
20160809_NGC4151-001R.fits	08/09/2016	129.6616	R	30	2.08
20160809_NGC4151-001V.fits	08/09/2016	129.6604	V	45	2.06
20160809_NGC4151-002B.fits	08/09/2016	129.6597	B	60	2.05
20160809_NGC4151-002I.fits	08/09/2016	129.6633	I	45	2.11
20160809_NGC4151-002R.fits	08/09/2016	129.6621	R	30	2.09
20160809_NGC4151-002V.fits	08/09/2016	129.6611	V	45	2.07
20160813_NGC4151-001B.fits	08/13/2016	133.6555	B	60	2.16
20160813_NGC4151-001I.fits	08/13/2016	133.6574	I	45	2.20
20160813_NGC4151-001R.fits	08/13/2016	133.6568	R	30	2.19
20160813_NGC4151-001V.fits	08/13/2016	133.6562	V	45	2.18
20160813_NGC4151-002B.fits	08/13/2016	133.6582	B	60	2.21
20160813_NGC4151-002I.fits	08/13/2016	133.6601	I	45	2.25

20160813_NGC4151-002R.fits	08/13/2016	133.6595	R	30	2.24
20160813_NGC4151-002V.fits	08/13/2016	133.6589	V	45	2.23
20160814_NGC4151-001B.fits	08/14/2016	134.6684	B	60	2.48
20160814_NGC4151-001I.fits	08/14/2016	134.6723	I	45	2.57
20160814_NGC4151-001R.fits	08/14/2016	134.6712	R	30	2.54
20160814_NGC4151-001V.fits	08/14/2016	134.6700	V	45	2.51
20160814_NGC4151-002B.fits	08/14/2016	134.6693	B	60	2.50
20160814_NGC4151-002I.fits	08/14/2016	134.6729	I	45	2.58
20160814_NGC4151-002R.fits	08/14/2016	134.6717	R	30	2.55
20160814_NGC4151-002V.fits	08/14/2016	134.6706	V	45	2.53

Appendix C

Code Used for Aligning Images

This is the code created by Dr. Jeffery used to align the images (Jeffery 2016).

```
#! /bin/csh -f

# clean up

rm *.mch

set files = `cat fitslist`
set mchfile = "test1.mch"

set n = $#files
set i = 1

while($i <= $n)
```

```
    # run daophot (find) to create a .coo file of all sources
    rm $files[$i].coo
    echo "11.5" > script
    echo "1.35" >> script
    echo "at" $files[$i]".fits" >> script
    echo "find" >> script
    echo "1,1" >> script
    echo $files[$i]".coo" >> script
    echo "y" >> script

    daophot < script

    @ i += 1

end

# run daomatch on all .coo files

set i = 2

echo $files[1].coo > script2
echo $mchfile >> script2

while($i <= $n)
    echo $files[$i].coo >> script2
```

```
    @ i += 1
end

daomatch < script2

# rm script*

awk '{print $3,$4}' $mchfile > shifts
```

Bibliography

Alard, C., & Lupton, R. H. 1998, The Astrophysical Journal, 503, 325

Bentz, M. C., et al. 2006, The American Astronomical Society, 651, 775

Carroll, B. W., & Ostlie, D. A. 2007, An Introduction to Modern Astrophysics, international edn. (San Francisco, CA: Pearson Education)

Chandra X-Ray Observatory. Accessed February 6, 2017, http://chandra.harvard.edu/photo/2011/n4151/

Collins, K. A., Kielkopf, J. F., Stassun, K. G., & Hessman, F. V. 2017, The Astronomical Journal, 153, 77

Couto, J. D., Kraemer, S. B., Turner, T. J., & Crenshaw, D. M. 2016, The Astrophysical Journal, 833, 1

Ghez, A. M., et al. 2002, The Astrophysical Journal, 689, 1044

Hintz, E. 2015, Private communication

—. 2017, Private communication

Holt, S. S., Mushotzky, R. F., Becker, R. H., Boldt, E. A., Serlemitsos, P. J., Szymkowiak, A. E., & White, N. E. 1980, The Astrophysical Journal, 241, L14

Jeffery, E. 2016, Private communication

Joner, M. 2017, Private communication

Keck, M. L., et al. 2015, The Astrophysical Journal, 806, 1

Peterson, B. 1997, An Introduction to Actve Galactic Nuclei, 1st edn. (Cambridge, UK: Cambridge University Press)

Peterson, B. M. 2003, ASP Conference Series, 290, 43

Ryden, B., & Peterson, B. M. 2010a, Foundations of Astrophysics, 1st edn. (Woodbury, NY: Pearson Addison-Wesley), 467–487

—. 2010b, Foundations of Astrophysics, 1st edn. (Woodbury, NY: Pearson Addison-Wesley), 489–508

Scheider, C. A., Rasband, W. S., & Eliceiri, K. W. 2012, Nature Methods, 9, 671

Schödel, R., et al. 2002, Nature, 419, 694

Slater, T. F., & Freedman, R. A. 2012, Investigating Astronomy, 1st edn. (New York: W. H. Freeman and Company), 361–364

Székely, P., Kiss, L. L., Jackson, R., Derekas, A., Csák, B., & Szatmáry, K. 2007, AA, 463, 589

Tody, D. 1993, ASP Conference Series, 52, 173

W. M. Keck Observatory. Accessed January 24, 2017, www.keckobservatory.org

Wildy, C., Landt, H., Goad, M. R., Ward, M., & Collinson, J. S. 2016, Monthly Notices of the Royal Astronomical Society, 461, 2085

Index